This article is a non-peer-reviewed preprint submitted to *EarthArXiv* in October 2025.
Please forward questions and feedback to mauricio.haag@mail.utoronto.ca

LONG-LIVED TOPOGRAPHY ALONG RIFTED MARGINS: INSIGHTS FROM APARADOS DA SERRA ESCARPMENT, SOUTHEAST BRAZIL

Mauricio B. Haag[1,2*], Scott Jess[2,3], Lindsay M. Schoenbohm[1,2], Eva Enkelmann[4], Taís F. Pinto[4]

[1] Department of Earth Sciences, University of Toronto, Toronto, ON, Canada

[2] Department of Chemical and Physical Sciences, University of Toronto Mississauga, Mississauga, ON, Canada

[3] School of the Environment, Washington State University, Pullman, WA, USA

[4] University of Calgary, Department of Earth, Energy, and Environment, Calgary, AB, Canada

Mauricio B. Haag (https://orcid.org/0000-0001-5038-4418)

Lindsay M. Schoenbohm (https://orcid.org/0000-0001-7898-356X)

Scott Jess (https://orcid.org/0000-0003-1960-2901)

Eva Enkelmann (https://orcid.org/0000-0002-1988-0760)

Taís F. Pinto (https://orcid.org/0009-0003-4762-9156)

GRAPHICAL ABSTRACT

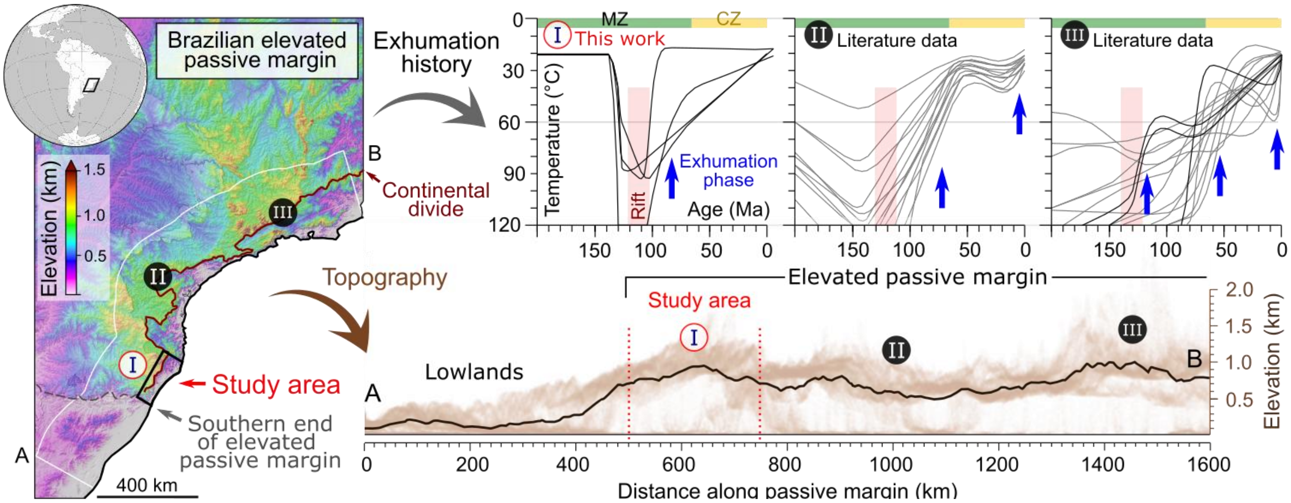

ABSTRACT

The Brazilian margin is one of the longest elevated passive margins (EPMs) in the world. However, both the timing of uplift and the long-term evolution of this EPM remain highly debated. In this study, we present a new suite of apatite (U-Th-Sm)/He (AHe) and fission track (AFT) ages for the southern end of the Brazilian EPM, in the Aparados da Serra plateau. Our results reveal that mean AHe ages range from 43 – 112 Ma, while AFT ages range from 46 – 222 Ma. Thermal history models suggest monotonic exhumation rates in the Aparados da Serra, with post-rifting rates < 50 m Myr-1 in the coastal plain and < 25 m Myr-1 in the volcanic plateau. Collectively, our results imply a total erosion of 2 – 4 km of material from the coast and < 2 km from the plateau since rifting ca. 120 – 100 Ma. AHe and AFT data indicate no detectable exhumation during the Cenozoic, implying that recent uplift along the margin was either absent or minimal, and that the relief observed in the Aparados da Serra is a likely consequence of sustained rift topography. Based on the absence of major recent tectonic events, we argue that Cenozoic exhumation patterns in the Aparados da Serra were largely controlled by geomorphologic processes (e.g., differential erosion). The spatial distribution of AHe ages indicates that the Aparados da Serra evolved through escarpment retreat, at least across the region extending from the present-day coastline to the escarpment position. Lastly, the equivalence between long (AFT and AHe) and short-term (catchment-averaged) erosion rates argues for sustained stability of the margin over geological timescales.

1 INTRODUCTION

Elevated passive margins (EPMs) represent the most dynamic regions within passive tectonic settings, featuring maximum erosion rates that are comparable to those in tectonically active regions (Wang et al., 2021). Despite significant research into the role of post-break-up deformation, uplift, and erosion along EPMs (e.g., Gallagher et al., 1994; van der Beek et al., 2002; Japsen et al., 2012; Braun, 2018; Hueck et al., 2019), fundamental questions about the timing of uplift and long-term geomorphic evolution of these settings remain controversial (Braun, 2018; Fonte-Boa et al., 2022). For example, while some authors argue for the preservation of rift topography through isostasy (e.g., Nielsen et al., 2009; Jess et al., 2019, 2020), others suggest that cyclic episodes of uplift, erosion, and peneplanation are needed to generate the rift-like topography observed along modern EPMs (e.g., Japsen et al., 2012; Green et al., 2022). In addition to these tectonic controls, the geomorphologic processes that govern the degradation of EPMs are still highly debated (van der Beek et al., 2002; Braun & van der Beek, 2004; Braun, 2018, see Fig. 7).

The southeast Brazilian continental margin comprises one of the longest EPMs on Earth (Fonte-Boa et al., 2022). This margin features a series of 1 – 3 km asl escarpment systems stretching for nearly 2,000 km along the South Atlantic coast (Fig. 1A), with striking structural and lithologic diversity (Fonte-Boa et al., 2022). The southern end of this system (south of lat. 28°S), hereafter named Aparados da Serra, is distinct from other segments of the EPM due to its extremely low-relief plateau (Fig. 1B-C) and absence of post-break-up volcanism or reactivation, which are common features along other parts of the Brazilian EPM (Riccomini et al., 1989; Cogné et al., 2012; Sacek et al., 2012; Fonte-Boa et al., 2022; Fonseca et al., 2023). Despite its unique characteristics, the exhumation history of the Aparados da Serra remains largely undersampled, as thermochronological studies have predominantly focused on the northern segment of the Brazilian EPM (Fig. 1D-E).

In this study, we present a novel suite of apatite (U-Th-Sm)/He (AHe) fission track (AFT) dates for the Aparados da Serra (Fig. 1E). Combined with geological observations, inverse thermal history models reveal protracted exhumation histories since rifting at ca. 120 - 100 Ma. Our thermal history model results also indicate no evidence of recent (Cenozoic) uplift, suggesting that the elevated topography of the Aparados da Serra has persisted since early Cretaceous rifting. Based on the spatial distribution of AHe ages, we also identify that the margin has likely evolved via progressive back cutting (escarpment retreat), although retreat velocity could not be determined.

2 GEOLOGICAL BACKGROUND

Located at the southern limit of the Brazilian EPM, the Aparados da Serra consists of a volcanic plateau (1.0 – 1.6 km asl) bounded to the east by a 200-km long NNE-SSW-trending escarpment (Fig. 2). From north to south, the escarpment morphology transitions from a simple, "divide-type escarpment" in which the divide and scarp edge are coincident and sub-linear to a more complex and sinuous "gorge-head type" escapement, marked by a series of embayments and deeply incised fluvial valleys (Fig. 2) (Haag et al. 2025b). This trend is accompanied by a decrease in the distance between the escarpment and the coast, which gradually declines from ~ 90 km in the north to 15 km in the south (Fig. 2).

Geological units are divided into three major groups along the Aparados da Serra, from older to recent: (i) underlying basement units include plutonic and metamorphic rocks (Ediacaran) of the Brazilian shield; (ii) overlying clastic (marine – fluvial) sedimentary rocks of the Paraná Basin (Lower Permian - Cretaceous); and (iii) capping effusive volcanics of the Paraná-Etendeka LIP (lower Cretaceous), locally grouped in the Serra Geral Group (Milani et al., 2007; Canile et al., 2016; Rossetti et al., 2018; Gomes & Vasconcelos, 2021; Scherer et al., 2023). In the study area, the escarpment is mainly composed of volcanic and sedimentary rocks, while basement units are restricted to the lower coastal domains. No younger lithological units have been identified overlying the plateau or along the escarpment face (Wildner 2008, 2014), which suggests ongoing erosion/non-deposition since rifting.

Tectonically, the study area evolved from an orogenic collisional setting (Pan-African/Brasiliano, Neoproterozoic) to a large intra-cratonic basin (Ordovician–Cretaceous), characterized by the deposition of thick sedimentary units of the Paraná Basin (Milani et al., 2007; Scherer et al., 2023). The geological record of the Paraná Basin is characterized by extensive periods of exhumation (e.g., Lower Triassic–Upper Jurassic), as indicated by several unconformities within the basin (Milani et al., 2007; Canile et al., 2016; Scherer et al., 2023). Relevant to this study, the late tectonic history (Cretaceous–Present) includes the emplacement of the Paraná-Etendeka LIP, resulting in the deposition of > 2 km of lavas (Milani et al., 2007; Rossetti et al., 2018; Gomes & Vasconcelos, 2021; Krob et al., 2019). The emplacement of the Paraná -Etendeka LIP was followed shortly by the opening of the South Atlantic through rifting, establishing a passive margin in the region at ~ 120 – 100 Ma (Contreras et al., 2010; Stica et al., 2014).

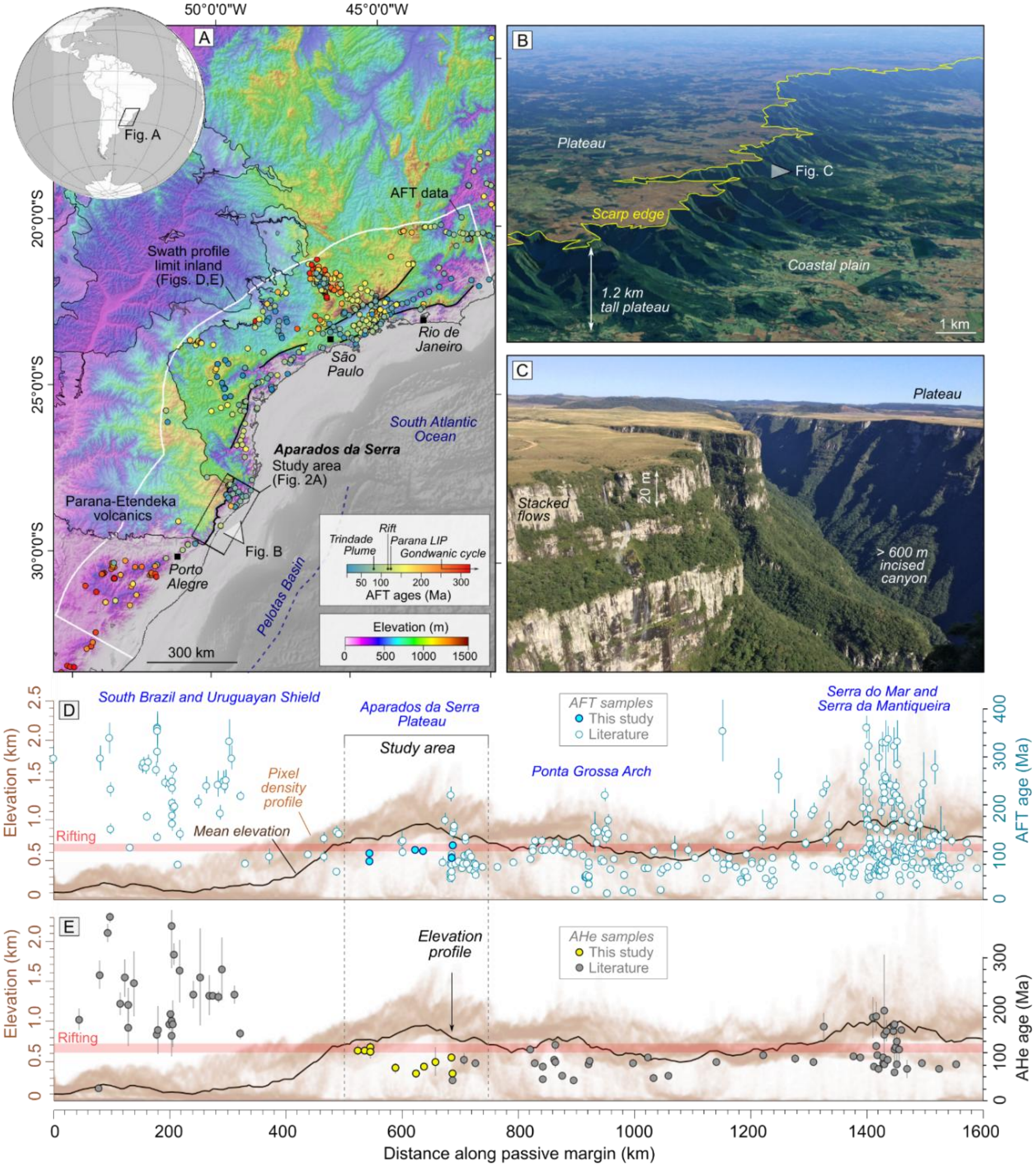

Figure 1 – A) Topographic setting of the southeast Brazilian passive margin and the available AFT cooling ages; B) GoogleEarth view of the central segment of Aparados da Serra; C) Field photo of deeply incised canyons along the south limit of the study area; D-E) 300-km wide elevation swath profile (left axis) along the passive margin, from the Uruguayan Shield to the Serra do Mar and Serra da Mantiqueira ridges, along with the available (D) AFT cooling ages (right axis) and (E) AHe cooling ages (right axis). The AFT panel includes data compiled from Krob et al. (2020), while AHe includes data from Karl et al. (2013), Krob et al. (2019), Cogné et al., (2011, 2012), Hueck et al. (2019), Machado et al. (2019, 2020), and Gezatt et al. (2021). In D and E, pixel density represents terrain elevation. The timing of rifting is indicated with a horizontal red line at an age of 100 - 120 Ma.

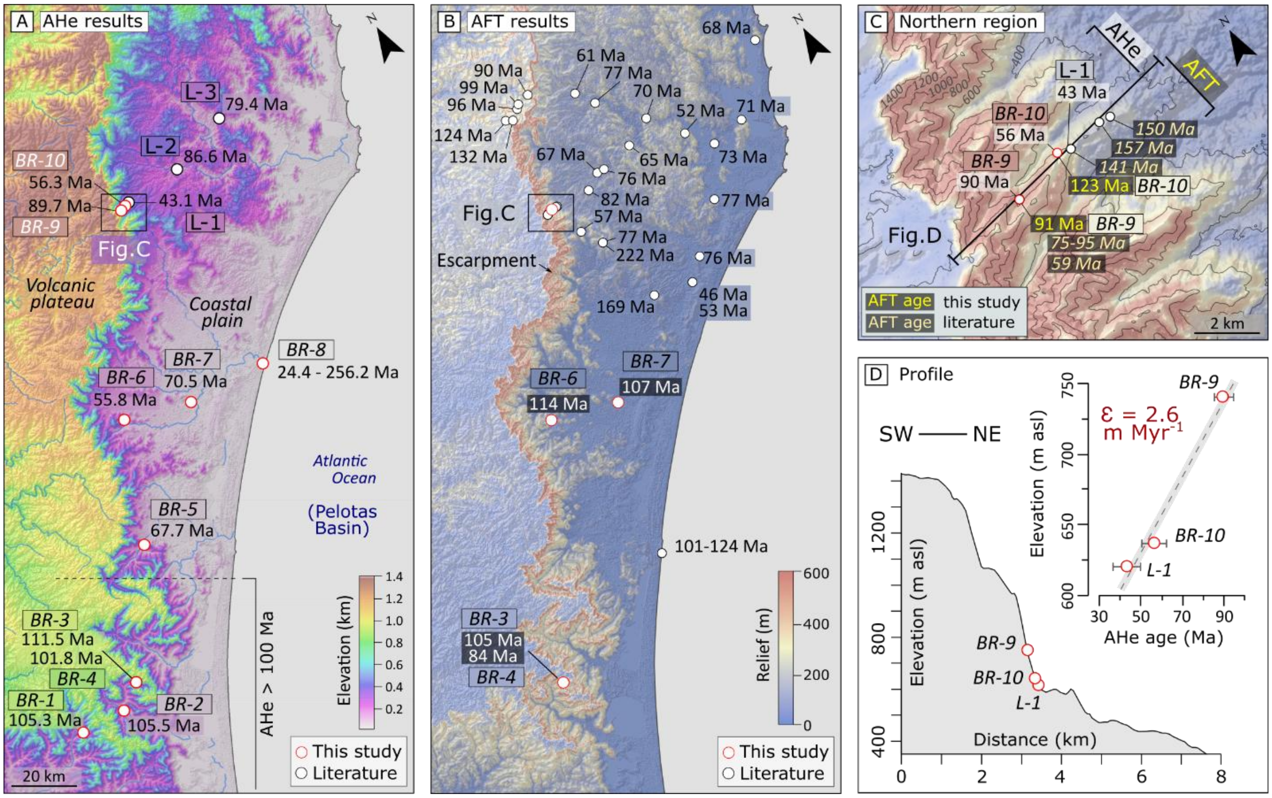

Figure 2 – A) Topography of the study area with the respective AHe cooling ages. B) Relief of the study area with respective available AFT central ages. C) Inset of the northern section of the study area (Rio do Rastro Profile) highlighting AHe and AFT ages; D) Cross section on escarpment edge with respective AHe sample locations. Samples from the literature include data from Gallagher et al. (1994), Karl et al. (2013), Krob et al. (2019) and Bicca et al. (2020).

3 METHODS

To resolve the exhumation history of the study area we combine apatite low-temperature thermochronology techniques (AHe and AFT) and thermal history modeling. All analytical procedures were performed at the Calgary Geo- and Thermochronology Laboratory of the University of Calgary and follow the methods summarized by McKay et al. (2021) for AHe analysis and Fraser et al. (2021) for AFT analysis.

3.1 Sampling strategy

Sampling focused on transects perpendicular to the escarpment face, along one elevation profile, and at several control points along the escarpment face and coastal plain

(Fig. 2A). In this contribution, all samples are collected from sedimentary units of the Paraná Basin, including: Botucatu Fm. (Early Cretaceous; medium to fine eolian sandstone; Scherer, 2000), with a depositional age of 134 – 145 Ma (Bertolini et al., 2020) and U-Pb peak in zircon provenance ages of Ediacaran age (Canile et al., 2016; Bertolini et al., 2021); and Rio do Rastro Fm. (Permian–Triassic; fine sandstones interbedded with siltstone and mudstones; Canile et al., 2016), with a depositional age of 250 – 280 Ma (Milani et al., 2007; Canile et al., 2016) and U-Pb zircon provenance of Ediacaran age (Canile et al., 2016). For details on sampling sites, please check SI1. For each sample, we collected 2 – 5 kg of material for mineral processing, which was performed at the University of Toronto Mississauga, following the approach of Donelick (2005). Please refer to SI2 for details on mineral separation.

In addition to our own AHe and AFT data, we also incorporate three AHe samples from Karl et al. (2013) and forty AFT samples from Gallagher et al. (1994), Karl et al. (2013), Krob et al. (2019), and Bicca et al. (2020). These studies include sedimentary samples from the Rio Bonito Fm. (Carboniferous–Permian; fine sandstones interbedded with siltstone and mudstones; Canile et al., 2016), volcanics from the Serra Geral Gr., as well as granitoid samples from basement rocks (Ediacaran).

3.2 Apatite (U-Th-Sm)/He

We focus on AHe analysis due to its low-temperature sensitivity with the partial retention zone for helium (HePRZ) ranging from 40 – 70°C (e.g., Flowers et al., 2009), suitable for analyzing near-surface (1 – 2 km) processes (e.g., van der Beek et al., 2002; Braun & van der Beek, 2004). In this contribution, we present AHe ages for a total of ten samples (Table 2). For each sample, whenever possible, we select well-formed, unbroken, inclusion-free crystals using a Stereo Microscope model ZEISS SteREO Discovery.V12 (SI3). We then picked five to seven crystals from this pool, recording each crystal's length, long width, short width, number of terminations, and surface aspects. Lastly, we packed individual grains in Nb tubes and performed the He extraction using an Applied Spectra Alphachron helium line, while parent isotopes (^{235}U, ^{238}U, ^{232}Th, and ^{147}Sm) were determined via isotope dilution (Evans et al., 2005).

We calculated ages using the Taylor expansion method and corrected for alpha ejection using the approach of Ketcham et al. (2011). Analytical results are reported in the SI3.

3.3 Apatite Fission Track

We selected six samples for AFT dating using laser ablation fission track analysis (LA-AFT) (Hasebe et al., 2004). AFT dating is sensitive to slightly higher temperatures with the fission track partial annealing zone (PAZ) ranging 60–120°C (e.g., Gallagher et al., 1998). We mounted and polished the selected samples, followed by standard etching protocol of 5.5M HNO_3 at 21°C for 20 seconds (Donelick, 2005). A detailed description of sample preparation is provided by Fraser et al. (2021). We aimed to date 30 grains per sample and measured the diameter of the track opening parallel to the c-axis (Dpar) to gain information on apatite kinetic parameters (Ketcham et al., 2007). The grains chosen for dating had homogeneous track distribution, no fractures and no inclusions. Spontaneous track counting was performed in a Zeiss AxioImager.M2m optical microscope equipped with an Autoscan System Pty. Ltd. Stage. Similarly, confined track lengths measurements were conducted and are reported in (SI4). U concentration measurement was performed using an Applied Spectra Resolution LR Laser Ablation System coupled to an Agilent 7700x Quadrupole ICP-MS. Ablation spots were 33µm in diameter and placed in the center of the area where spontaneous tracks were counted. The fission track ages were calculated and zeta calibrated using the equations outlined by Hasebe et al. (2004, 2013). Durango apatite standards were frequently analyzed throughout the laser ablation session to ensure proper zeta calculation. Additionally, NIST610 was analyzed for calculation of uranium concentrations. Complete AFT data analysis results (analytical results, radial plots, length measurements and Dpar) are reported in SI4.

3.4 Thermal history modelling

We combined AHe and AFT cooling ages, track length, compositional data, and independent geological constraints to perform inverse thermal history modeling using *QTQt* 5.8.6 (Gallagher, 2012). *QTQt* uses a Markov Chain Monte Carlo (MCMC) approach to obtain a set of “acceptable” thermal histories. For each model, we secure algorithm stability by performing runs with at least 1 million iterations, ensuring a steady likelihood chain (Gallagher, 2012). Additionally, samples located within the same region and without evidence of tectonic displacement (e.g., BR-9, 10 and L-1; Fig. 5A) are modelled as a group. Thermal histories modelling was only completed on samples with both AFT and AHe data (BR-3, 4, 6, 7, 9, and 10), or on those AHe samples that could be included in a joint inversion with other samples (e.g., BR-1, 2, and L-1). Initial modeling attempts using exclusively AHe data (BR-5 and 8) revealed data dispersion that was too high to yield meaningful results.

Table 1 – Inputs for the thermal model. H_P indicates the plateau elevation, while H_S the sample elevation.

Timing	Event Class	Affected units	Temperature	References
0 Ma	Present day temperature	All units	20 ± 10 °C	Wygrala (1989)
133 ± 1 Ma	Depositional	Serra Geral Gr. (Paraná-Etendeka LIP)	$T_{MIN} = (H_P - H_S) \times 30°C$ T_{MAX} = Unconstrained	Gomes & Vasconcelos (2021)
140 ± 6 Ma	Depositional	Botucatu Fm.	20 ± 10 °C	Milani et al. (2007); Canile et al. (2016); Bertolini et al. (2020).
	Exhumation	Rio do Rastro Fm.		
265 ± 15 Ma	Depositional	Rio do Rastro Fm.	20 ± 10 °C	
580 ± 80 Ma	Provenance	All sedimentary units	800 ± 200 °C	

We performed joint inversion of AFT and AHe data using the annealing model of Ketcham et al. (2007). Single-grain AHe age dispersion is expected in detrital samples that may have experienced prolonged residence in the HePRZ (e.g., Jess et al., 2019). Considering that all samples in our dataset are detrital and likely resided for extended periods within the HePRZ (Gallagher et al., 1994; Karl et al., 2013; Krob et al., 2019; Bicca et al., 2020), we implemented additional steps to better account for kinetic variability in thermal modeling: (i) we applied the radiation damage model (Recanati et al., 2017) to account for changes in helium diffusivity, and (ii) we resampled the additional activation energy (ΔE_b) required for diffusion of helium trapped in damage vacancies (Gautheron et al., 2009, 2012; Gerin et al., 2017). Accordingly, while the radiation damage model seeks to compensate for changes in diffusion kinetics, resampling ΔE_b between 20 – 50 kJ mol^{-1} seeks to improve model predictions by accounting for different apatite composition and damage (Gerin et al., 2017). See SI6 for further details in inverse thermal history modelling.

The Paraná Basin has been extensively studied due to the presence of mineral resources including coal and gas (e.g., Milani et al., 2007; Bicca et al., 2020). This detailed tectonic and stratigraphic framework allows us to independently constrain thermal events, including depositional and exhumation periods outlined in Table 1. The present-day geothermal gradient in the study area ranges from 30 – 35°C km^{-1} (Vieira & Hamza, 2019) but was likely higher during the emplacement of the Paraná-Etendeka LIP and subsequent rifting. Accordingly, total overburden and erosion rates are estimated from cooling rates using geothermal gradient from 30 – 40°C km^{-1}.

4 RESULTS

We report a total of 51 new AHe dates from ten samples and AFT dates from six samples (Table 2). Single-grain AHe data range from 18 – 254 Ma, while mean AHe sample ages range 56 – 111 Ma. AFT central ages range from 84 – 1235 Ma, with MTL of 13.31 – 14.38 μm and Dpar of 1.93 – 2.66 μm (Table 2). All AFT samples show high dispersion with P (χ^2) < 0.05.

4.1 Apatite low-temperature thermochronology

Including data from Karl et al. (2013), the mean AHe sample ages range from 43 – 112 Ma (Fig. 3B, SI7) in the study area. We group AHe data based on their sampling location (Fig. 3A):

(i) **Deep-incised valleys** (four samples, BR-1 to 4): samples located at low elevations landward of the escarpment crest, at the bottom of narrow and deep fluvial valleys cut into the plateau and located in the southern part of the study area (Fig. 2A, 3A). These samples are typically older (~ rift age), with mean AHe ages ranging 102 – 111 Ma (Fig. 3B).

(ii) **Escarpment face** (three samples, BR-9, 10 and L-1): collected on the escarpment face (Fig. 2A, 3A), these samples display a wide range of mean AHe ages from 43 – 90 Ma (Karl et al., 2013) and are younger than rifting (< rift age) (Fig. 3B). These samples show a positive correlation between sample elevation and AHe age (Fig. 2D).

(iii) **Coastal plain** (six samples, BR-5 to 8, L2 and L3): collected between the coastline and the escarpment foot (Fig. 2A, 3A), these samples also feature variable ages and are relatively young (< rift age), with mean AHe ages from 56 – 87 Ma (Karl et al., 2013) (Fig. 3B). Spatially, AHe ages are marked by a younging trend from the coast toward the escarpment, although significant variability is present (Fig. 3B).

Combined with samples from the literature (Gallagher et al. 1994; Karl et al. 2013; Krob et al. 2019; Bicca et al. 2020; SI7), AFT central ages range from 46 – 222 Ma, without a distinct spatial distribution (Fig. 3C, 4B). MTLs range from 10.3 to 15.1 μm (Fig. 4C); overall, volcanic samples from higher elevations, reported by Gallagher et al. (1994) feature longer length measurements (MTL > 14.1 μm), while sedimentary and basement samples show a spread of MTL values from 12.3 – 14.4 μm (Fig. 4C, SI7).

Table 2 – Thermochronology results. Sample elevation, stratigraphic age, and the distance to the coastline. For AHe and AFT results, N represents the number of grains analyzed; For track length results, N represents the number of measured tracks. MTL results are reported as corrected for c-axis. For AHe data, a complete table with analytical results, grain measurements, uncorrected ages and Ft correction is reported in SI3. For AFT data, analytical results, radial plots, MTL and Dpar measurements are reported in SI4.

Sample information				AHe results (corrected)			AFT results			Track length results		
Lithologic unit	Sample ID	Z (m asl)	Distance to coast (km)	N	Min – Max (Ma)	Mean age ± σ1 (Ma)	N	Central age ± σ1 error (Ma)	Dispersion	N	Projected MTL ± σ1 (µm)	Dpar ± σ1 (µm)
Botucatu Fm. Early Cretaceous	BR-1	145	40	5	74 – 131	105.3 ± 10.8	-	-		-	-	-
	BR-2	71	29	5	82 – 130	105.5 ± 8.2	-	-		-	-	-
	BR-3*	261	27	5	75 – 154	111.5 ± 13.2	28	105 ± 12	23%	32	13.31 ± 0.25	2.14 ± 0.29
	BR-4	260	27	4	18 – 122	101.7 ± 14.1	30	84 ± 14	40%	12	14.15 ± 0.23	1.93 ± 0.15
	BR-5	127	30	4	45 – 197	67.7 ± 10.0	-	-		-	-	
	BR-9*	740	50	5	78 – 106	89.7 ± 4.6	29	91 ± 11	28%	46	14.16 ± 0.13	2.21 ± 0.18
Rio do Rastro Fm. Upper Permian	BR-6	131	41	4	44 – 161	55.7 ± 8.0	26	114 ± 18	33%	95	14.27 ± 0.11	2.33 ± 0.44
	BR-7	12	21	3	32 – 75	70.5 ± 2.7	32	107 ± 17	39%	54	14.38 ± 0.14	2.66 ± 0.43
	BR-8	30	1	7	24 – 254	-	-	-		-	-	-
	BR-10	637	49	5	43 – 76	53.6 ± 6.0	17	123 ± 12	30%	70	13.72 ± 0.16	2.35 ± 0.32

* Samples collected within 1 m of the lava-sandstone contact.

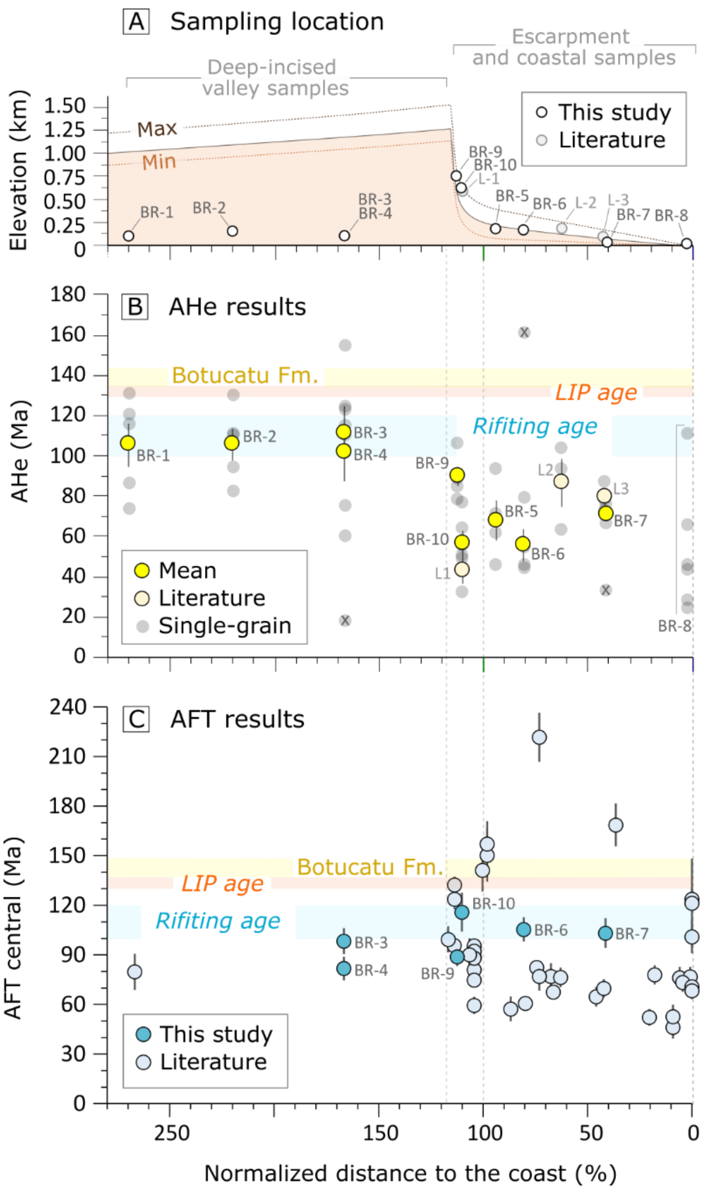

Figure 3 – Geographic distribution of AHe and AFT ages. A) Generalized, present-day escarpment morphology with sample location and altitude. B) Mean AHe cooling ages. C) AFT central ages. The main tectonic and depositional events are represented in B-C by horizontal bars and include the deposition of Botucatu Formation ca. 140 Ma (Bertolini et al., 2020), the Paraná-Etendeka LIP lavas ca. 133 Ma (Gomes and Vasconcelos, 2021), the opening of the South Atlantic Ocean ca. 120 – 100 Ma (Stica et al., 2014). The samples from the literature include data from Gallagher et al. (1994), Karl et al. (2013), Krob et al. (2019), and Bicca et al. (2020).

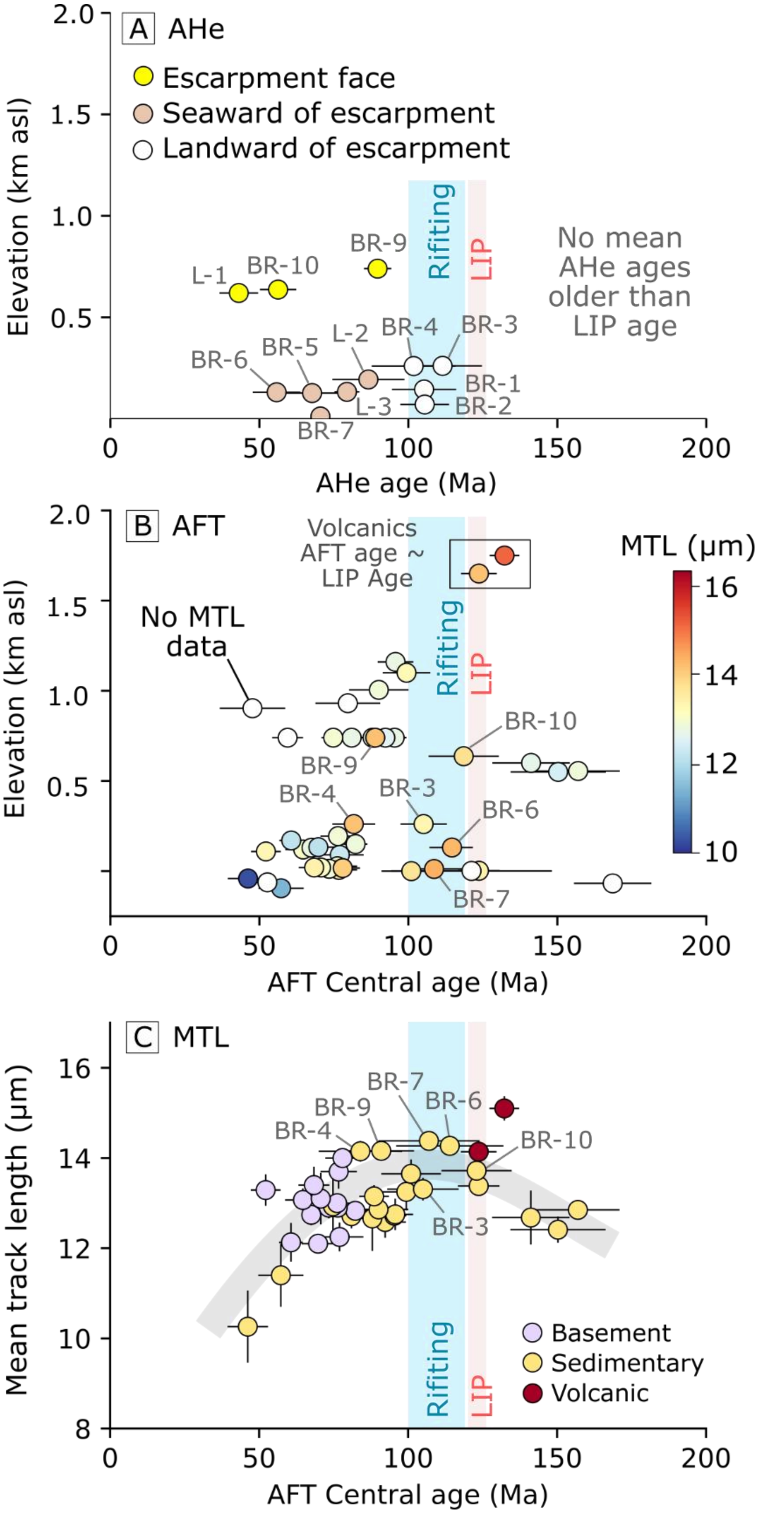

Figure 4 – AHe and AFT results according to elevation. A) Mean AHe age, color-coded by location. B) AFT central ages color-coded by MTL. C) AFT central ages vs. MTL results ("boomerang" plot), color-coded by lithology. B and C include data from Gallagher et al. (1994), Karl et al. (2013), Krob et al. (2019), and Bicca et al. (2020).

4.2 Thermal history modelling

Collectively, all joint (AHe and AFT) models (Figs. 5D-G) are consistent with a discrete temperature increase of ~ 70 – 90 °C at the time of the LIP emplacement ca. 133 Ma (Fig. 5B). Following this temperature increase, modeling results reveal an accelerated cooling phase from 120 – 90 Ma (1 – 9 °C Myr^{-1}; Fig. 5C). This cooling phase is followed by slow, protracted cooling during the post-rift period in the Late Cretaceous throughout the Cenozoic. Overall, post-rifting (100 – 66 Ma) cooling rates are < 3 °C Myr^{-1}, while Cenozoic rates indicate near-surface temperatures with maximum cooling rates of < 1 °C Myr^{-1} (Fig. 5C).

5 DISCUSSION

5.1 Heating events

In the study area, single-grain AHe cooling ages range from 17 to 254 Ma, with ~ 95% of all dated grains younger than the Paraná-Etendeka LIP emplacement (Fig. 3B, SI5). In contrast, AFT central ages range from 46 to 222 Ma, with 82% of central ages postdating the LIP (Fig. 3C, SI5) (Gallagher et al., 1994; Karl et al., 2013; Krob et al., 2019; Bicca et al., 2020). This indicates that the high thermal flux associated with the LIP, likely in combination with significant overburden, was sufficient to fully reset nearly all AHe dates in the study site (e.g., Hueck et al., 2018). However, the AFT system was only partially reset, consistent with previous results from sedimentary samples analyzed by Gallagher et al. (1994), which suggest a limited sensitivity of AFT to post-LIP thermal events. This observation is supported by the notable dispersion observed in AFT dates (Table 2).

All AFT central ages are younger than the depositional age of the Rio do Rastro Fm. (~ 250 Ma, SI5), therefore matching the Gondwana I subsidence cycle of the Paraná Basin (Canile et al., 2016). Collectively, these results suggest that thermal effects associated with both the Gondwana I depositional cycle (~190 Ma) and the later emplacement of the Serra Geral Group/Paraná-Etendeka LIP (~133 Ma) played an important role in annealing and resetting apatite ages in the Aparados da Serra region. These observations are supported by inverse thermal history modeling results, which are consistent with a notable temperature increase at ~133 Ma in all modelled samples (Fig. 5). Therefore, our analyses support the hypothesis of widespread heating/burial associated with the emplacement of the Paraná-Etendeka LIP (Gallagher et al., 1994; Hueck et al., 2018). Based on inverse thermal history models, we observe cooling paths compatible with a minimum temperature increase of ~ 65 – 95 °C for joint (AFT and AHe) models, equivalent to a minimum overburden of ~ 1.6 – 2.3 km of rock material if we consider a geothermal gradient between 30 and 40 °C km^{-1} (Fig. 5B). These values agree with overburden estimates obtained by previous studies in the Aparados da Serra (ca. 2.5 km; Gallagher et al., 1994; Karl et al., 2013; Hueck et al., 2019; Krob et al., 2019; Bicca et al., 2020).

Thermochronology results from other regions affected by LIPs support the discrete heating pattern observed in our study area. For instance, Colleps et al. (2021) demonstrated that the Deccan Traps experienced a distinct thermal pulse, likely reflecting a significant thermal overprint caused by elevated regional heat flow, increased overburden, or a combination of both. Similarly, the emplacement of extensive dike swarms, sills, and thick volcanic flows, features commonly associated with LIPs and rifted margins, are suggested to substantially increase local geothermal gradients (Nyblade & Sleep, 2003; Krob et al., 2020). Consequently, both spatially and temporally variable geothermal gradients are expected across regions affected by LIPs (e.g., Nyblade & Sleep, 2003). Therefore, it is important to note that the interpretations presented in this study do not fully account for these heterogeneities, which could influence the inferred thermal histories.

5.2 Exhumation rates

Joint inverse thermal history models suggest protracted exhumation histories in the Aparados da Serra coastal plain since rifting ca. 120 – 100 Ma (Fig. 5). For geothermal gradients of 30 – 40 °C km^{-1}, modeled samples indicate exhumation rates of ~ 50 m Myr^{-1} for the Late Cretaceous, although peaks of accelerated exhumation between 100 – 300 m Myr^{-1} are observed in two samples at ~ 110 Ma (BR-3 and BR-4, Fig. 6B). In the Cenozoic, all modeled samples reveal exhumation rates < 25 m Myr^{-1} (Fig. 6B). For the coastal plain region

(BR-6 and 7), modelled Cenozoic rates of < 20 m Myr^{-1} are within the same order of magnitude as low-temperature thermochronology (AHe + AFT) results obtained by Karl et al. (2013) and Krob et al. (2019), who documented rates of ~ 12 m Myr^{-1} and 23 – 68 m Myr^{-1}, respectively. Modelled Cenozoic rates are also comparable to short-term erosion rates obtained using terrestrial cosmogenic nuclides (TCNs) in escarpment-draining rivers from the Aparados da Serra (5 – 136 m Myr^{-1}; Haag et al., 2025a).

Samples collected landward of the escarpment (South group, samples BR-1 to 4) are considered to be potentially representative of plateau erosion rates. Modelled rates of these samples suggest an accelerated phase of exhumation up to 300 m Myr^{-1} from ca. 115 – 95 Ma, followed by protracted, low exhumation rates of < 10 m Myr^{-1} from 90 Ma to present (Fig. 6B). Based on their present-day elevation (> 600 m asl), samples collected along the escarpment face (North group, samples BR-9, 10 and L-1) are also considered as potentially representative of erosion rates in the plateau. Similar to BR-1 to 4, north group samples feature an accelerated exhumation phase up to 40 m Myr^{-1} from 105 – 90 Ma (Fig. 6B). An elevation profile using mean AHe ages (samples BR-9, BR-10 from this study and L-1 from Krob et al., 2019) indicates exhumation rates of the plateau of only 2.6 m Myr^{-1} from 90 – 40 Ma (Fig. 2D). In contrast, modelled rates for the same period using the same samples indicate slightly higher exhumation rates of 16 – 22 m Myr^{-1} (Fig. 6B). These rates are in agreement with TCN-derived erosion rates of 6 m Myr^{-1} for plateau-draining rivers in the study area (Haag et al., 2025a). They also match the expected short-term erosion rates of other EPMs plateaus, including south and western Africa (Makhubela et al., 2021), eastern Australia (Codilean et al., 2021), western Madagascar (Wang and Willett, 2021; Brosens et al., 2023), and western India (Mandal et al., 2015), where TCN rates range from 2.7 to 47 m Myr^{-1}.

Collectively, these results demonstrate that the Aparados da Serra have experienced remarkably low erosion rates throughout the Cenozoic. The persistence of such low denudation underscores the long-term stability of the volcanic plateau and associated escarpment. Building on these results, the following section explores the potential mechanisms that may account for the long-term uplift of the study area.

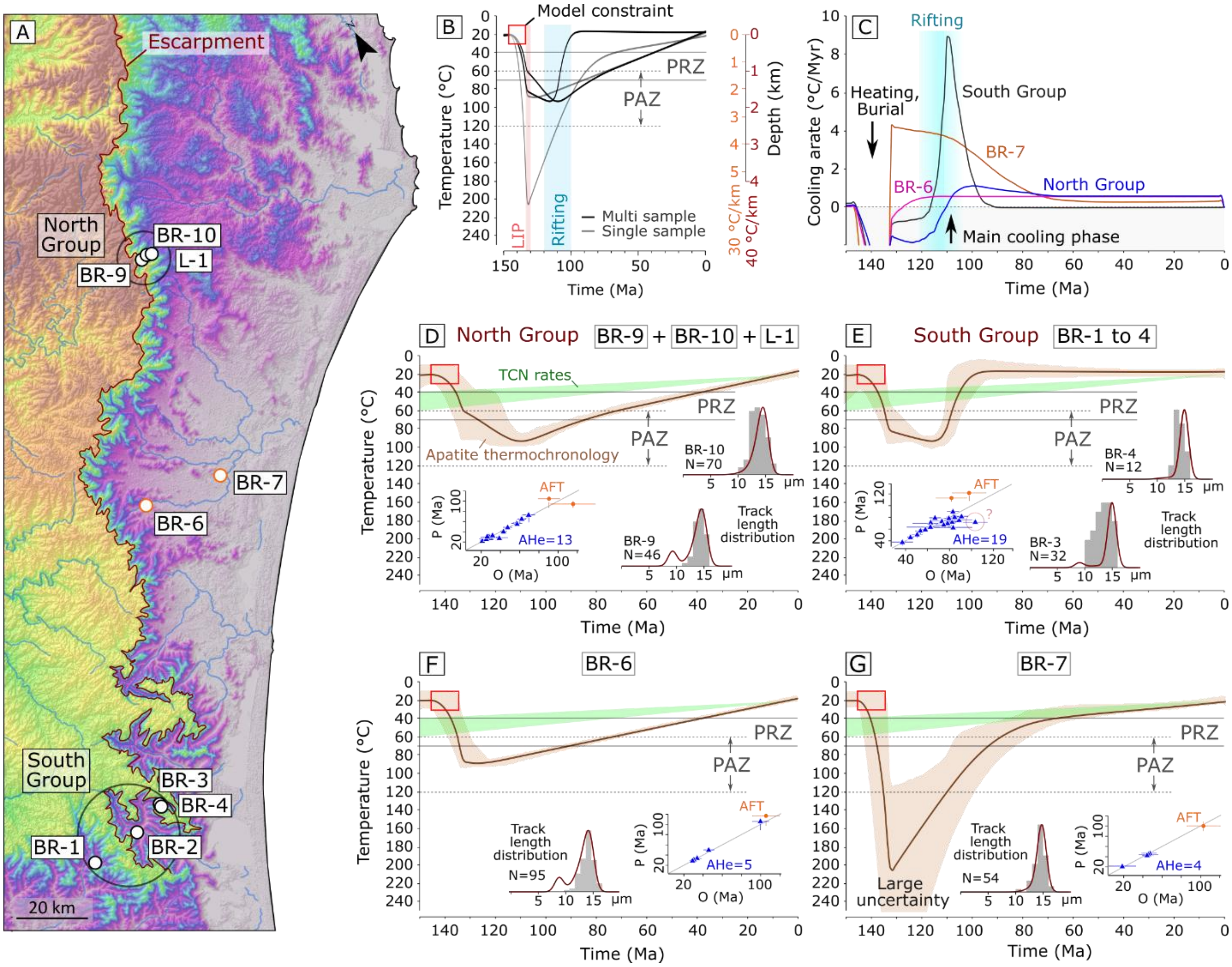

Figure 5 – Inverse thermal history modeling results for samples from the Aparados da Serra escarpment. A) Overview of sampling sites. B) Summary of cooling paths for modelled samples and expected burial depths for 30 and 40 °C km^{-1} geothermal gradients. C) Summary of cooling rates calculated based on modelled cooling paths presented in (B). D-G) Model results: The brown line in each panel represents the expected thermal history model, while the shaded brown area denotes the 95% confidence interval. Green areas show projected terrestrial cosmogenic nuclide (TCN) erosion rates measured on the Aparados da Serra Plateau (Haag et al., 2025a). Note that TCN rates integrate over short timescales of <1 Myr and are not representative beyond this interval; accordingly, TCN rates are projected further back in time for illustrative purposes only. Measured track length distributions are shown as grey histograms, with predicted track length distributions in maroon. Observed (O) and predicted (P) AFT central ages are shown as orange circles (•), as single-grain AHe ages are shown as blue triangles (▲).

5.3 Timing of uplift and potential mechanisms

Thermal history model results suggest relatively low and uniform exhumation rates across the Aparados da Serra since rifting (Fig. 5C, 6B). These findings are supported by previous studies conducted in the study region (Gallagher et al., 1994; Karl et al., 2013; Krob et al., 2019; Bicca et al., 2020), which document protracted erosion from the Late Cretaceous to the present. Furthermore, the consistency in erosion and exhumation rates across multiple techniques with contrasting temporal resolutions (AFT, AHe, and TCNs; Haag et al., 2025a) further supports the interpretation of slow, protracted denudation throughout the Cenozoic. Combined, these observations indicate that the timing of uplift was likely contemporaneous with continental rifting and/or LIP emplacement (Fig. 6A, B), and that the Aparados da Serra has since undergone protracted topographic decay (e.g., Nielsen et al., 2009; Jess et al., 2019) rather than recent tectonic rejuvenation (e.g., Japsen et al., 2012).

Curiously, we observe no apparent relationship between modeled exhumation rates, climate records (Veizer et al., 1999; Mills et al., 2019), sediment flux into the Pelotas Basin (Contreras et al., 2010; Rohais et al., 2021), mid-Atlantic ridge spreading rates (Clark, 2018), and Andean convergence rates (Horton, 2018) (Fig. 6B-F). This decoupling suggests that the influence of far-field stresses, whether from the Andean orogeny or the Atlantic mid-ocean ridge, on exhumation in the Aparados da Serra region has been limited, or possibly too subtle to detect with low-temperature thermochronology (e.g., Contreras et al., 2010; Rohais et al., 2021). Even though sedimentary fluxes have been used to infer uplift and exhumation events in various passive margin settings (e.g., Baby et al., 2018), here we also observe no relationship between tectonics and sedimentary input into the Pelotas Basin. In this basin, major unconformities are primarily associated with eustatic sea-level fluctuations (Contreras et al., 2010), rather than tectonic activity.

Based on the comprehensive chart presented in Fig. 6, the Paraná-Etendeka LIP and subsequent continental rifting were likely the last major events capable of influencing low-temperature thermochronology systems in the Aparados da Serra. These events also appear to be the most recent drivers of regional uplift in the Aparados da Serra. Particularly relevant to the establishment of permanent uplift, extensive evidence of magmatic underplating in southeast Brazil suggests that this process may have played a key role in generating elevated topography (Bernardes et al., 2023). Therefore, the Cenozoic evolution of the Aparados da Serra greatly contrasts with other parts of the Brazilian EPM, where tectonic reactivation is locally present (Riccomini et al., 1989; Cogné et al., 2012; Sacek et al., 2012; Fonte-Boa et al., 2022; Fonseca et al., 2023).

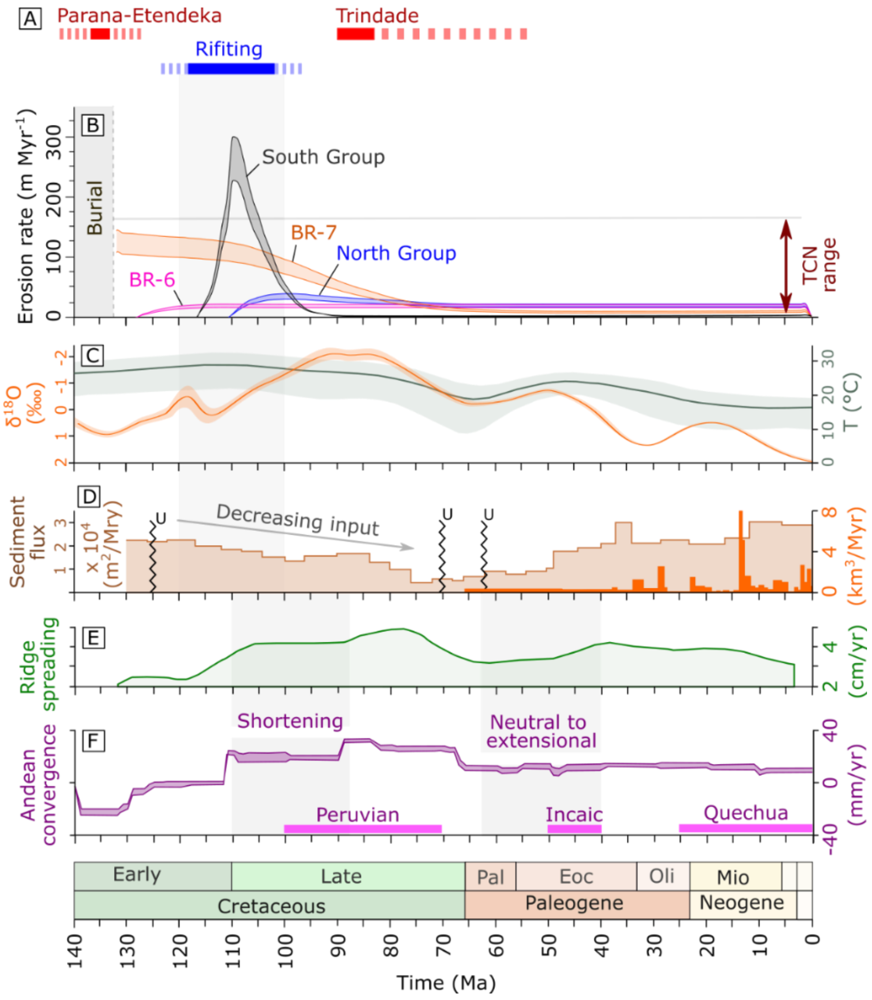

Figure 6 – Apatite low-temperature thermochronology exhumation rates for the Aparados da Serra compared to stratigraphic records and tectonic events in South America. A) Major tectono-magmatic events in eastern South America (Thompson et al., 1998; Gibson et al., 1999; Maia et al., 2021; Gomes and Vasconcelos, 2021 and references therein). B) Exhumation rates calculated for geothermal gradients 30 – 40 °C km^{-1}. C) Global climate record (Veizer et al., 1999 for δ^{18}O record (in parts per thousand = ‰) and Mills et al., 2019 for surface

temperature). D) Sediment flux (light orange) is from offshore sedimentary record of the *Pelotas* Basin (depocenter of the study area), including calibrated sedimentary input and erosional shelf unconformities (U) (light brown, Contreras et al., 2010) and high-resolution Cenozoic data (dark orange, Rohais et al., 2021). E) South Atlantic mid-ocean ridge spreading rates (green curve, Clark, 2018). F) Andean convergence velocity (purple curve, Horton, 2018) and phases (dark pink bars, Cobbold et al., 2001).

5.4 Geomorphologic evolution

In addition to the timing and origin of topography along the study area, the spatial distribution of AFT and AHe ages, and their modelled rates, allow us to evaluate the long-term geomorphologic evolution of the southern Brazilian EPM. While the denudation of EPMs can evolve via several pathways (Gallagher et al., 1998), two end-member scenarios are generally recognized: (i) escarpment retreat and (ii) plateau degradation (Brown et al., 2002; van der Beek et al., 2002; Braun and van der Beek, 2004). The escarpment retreat model suggests a drainage divide that coincides with the rift line and progressively migrates landward by escarpment back cutting (Fig. 7A) (van der Beek et al., 2002). In contrast, the plateau degradation model assumes a drainage divide located several tens of kilometers landward of the rift line; in this scenario, a fast period of erosion is focused on the region between the divide and the rift axis (Fig. 7B) (van der Beek et al., 2002).

Geodynamic conditions potentially favor the use of AHe for discriminating between these two scenarios in the study area. Low to moderate values of effective elastic thickness of the lithosphere (~ 10 – 40 km; Tassara et al., 2007), high geothermal gradients (30 – 35°C Km^{-1}, but likely higher in the past; Vieira and Hamza, 2019), and sufficient inland migration of the escarpment (migration distance ≥ characteristic wavelength of flexural deflection, which ranges from 30 – 80 km in the study area; Haag et al., 2025b) all point to a likely flexural response to erosion and therefore a detectable AHe trend along the coastal plain (Braun and van der Beek, 2004). However, the moderate elevation of the Aparados da Serra escarpment (1–1.6 km asl) places it at the lower limit for detecting escarpment retreat using AHe data (Braun and van der Beek, 2004).

Following the modeling results of Braun and van der Beek (2004), we compare our AHe data with the expected distribution of AHe dates for the escarpment retreat and the plateau degradation denudation scenarios (Fig. 7C, D). For this comparison, we normalized sample locations to the coastline-escarpment bottom segment, as well as all AHe to the rifting age, which is 100 Ma in the models of Braun and van der Beek (2004) and ~ 110 Ma in the Aparados da Serra (Stica et al., 2014). This comparison reveals that AHe ages from the coastal region of the Aparados da Serra are significantly younger than those predicted in the plateau degradation scenario (Fig. 7C). In this geomorphic evolution pathway, AHe dates on the coastal plain are expected to be 25 – 50% older than rifting (Fig. 7D; Braun and van der Beek, 2004). This is not observed in the AHe dates reported in the Aparados da Serra, which are generally 25 – 70% younger than the rifting. Accordingly, the spatial distribution of AHe dates appears to favor the escarpment retreat hypothesis, characterized by (i) a progressive decrease of AHe ages toward the escarpment bottom and (ii) ages that are typically younger than rifting (Fig. 7D) (Braun and van der Beek, 2004).

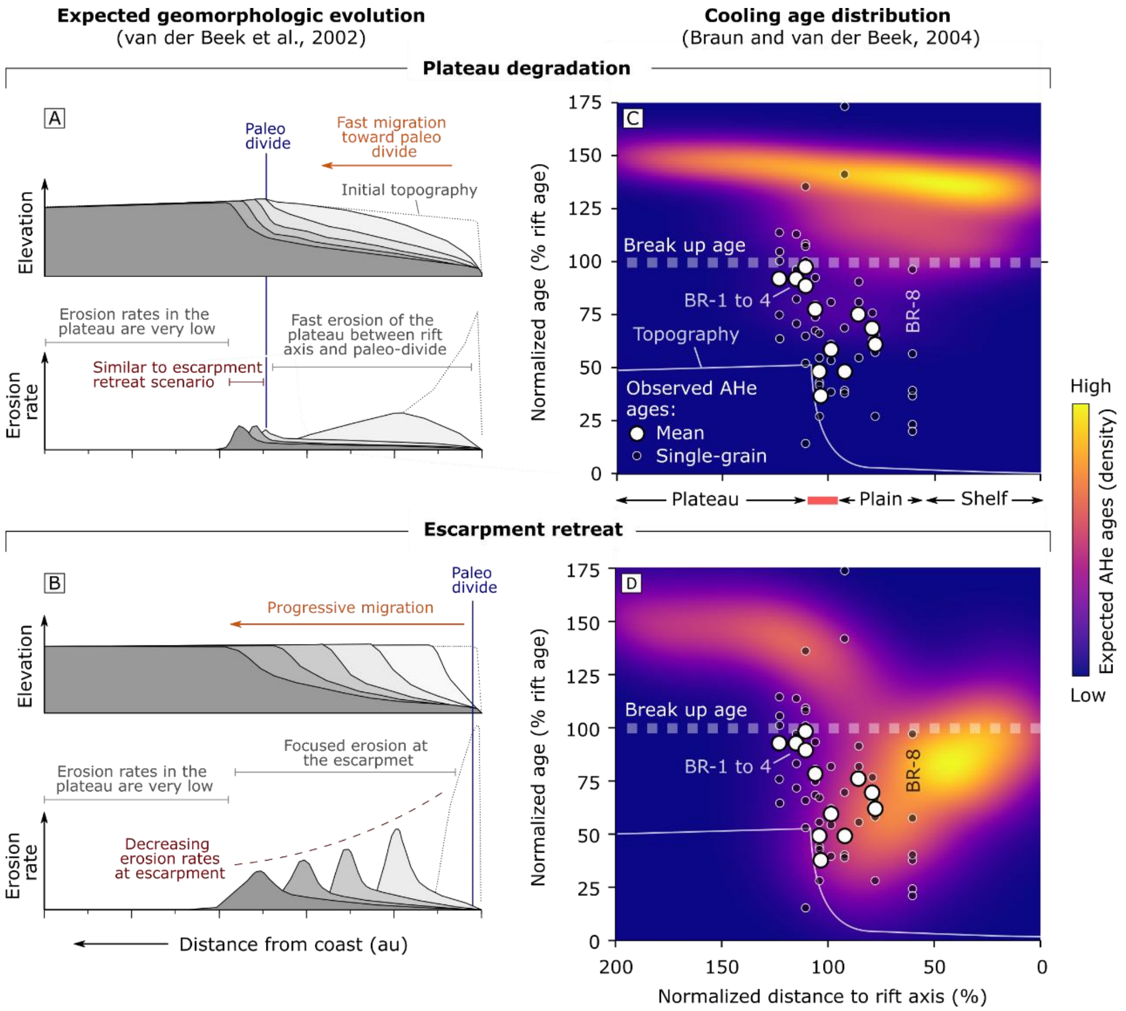

Figure 7 – Exhumation patterns expected for the (A, C) plateau degradation and (B, D) escarpment retreat scenarios with the respective locus of erosion since rifting. Geomorphological evolution is based on modeling results from van der Beek (2002), while the expected distribution of AHe ages is based on Braun and van der Beek (2004). Elevation and erosion rates in the left-side plot are arbitrary.

Although the spatial pattern of AHe ages appears consistent with an escarpment retreat model, quantifying retreat rates remains challenging with the available number of samples. For an effective elastic thickness ranging between ~10 and 40 km (Tassara et al., 2007), the minimum AHe ages are expected to be larger than escarpment stabilization times (Braun and van der Beek, 2004). Therefore, minimum observed AHe ages of approximately ~55 Ma only provide a first-order estimate for the timing of escarpment stabilization in the Aparados da Serra. Additionally, despite the overall spatial pattern supporting the escarpment retreat scenario, inverse thermal history models for samples collected along the coastal plain (Fig. 5; BR-6 and BR-7) do not exhibit a distinct, accelerated phase of exhumation expected in response to an erosional wave due to escarpment migration (Fig. 7B). Instead, the modeled samples indicate relatively steady and prolonged cooling, compatible with gradual plateau denudation (Fig. 5). In this context, the lack of an exhumation pulse may imply that the coastal plain experienced subdued erosional dynamics, or that any signal of rapid retreat has been thermally overprinted or spatially averaged out. Alternatively, it may also indicate that the exhumation caused by the migrating escarpment was not significant enough to result in a detectable signal in the thermal models. Therefore, while the AHe age distribution apparently supports the escarpment retreat model, the absence of a sharp exhumation event in inverse models (Fig. 5) highlights the complexity of interpreting low-temperature thermochronologic data in passive margin settings (Braun and van der Beek, 2004).

6 CONCLUSIONS

In this study we present novel AHe and AFT data for the southern end of the Brazilian elevated passive margin. Based on cooling ages, geological, and thermal history model observations, we identify that:

- The Aparados da Serra is marked by monotonic, slow cooling rates typically < 50 m $\mathrm{Myr^{-1}}$. These rates are compatible with recently obtained, short term, TCN erosion rates (Haag et al., 2025a).
- Thermal histories show no evidence of recent accelerated cooling episodes, implying either an absent or undetectable Cenozoic uplift in the study area. Therefore, the elevated topography observed in the Aparados da Serra EPM was likely achieved during rifting at ca. 120 – 100 Ma.
- The spatial distribution of AHe dates favours the escarpment retreat hypothesis for the geomorphic evolution of the Aparados da Serra, in which the divide progressively migrates away from the rift line over time. This hypothesis, however, is not supported by inverse models, which show not particular erosional wave.

ACKNOWLEDGMENTS & FUNDING

We thank Joshua Wolpert for his assistance in the field during sample collection, and Kerry Gallagher and David Peate for sharing their sampling strategies and site locations in southeast Brazil. This work was partially funded with an NSERC Discovery Grant awarded to L.M.S.

REFERENCES

Assumpção, M., James, D., Snoke, A., 2002. Crustal thicknesses in SE Brazilian Shield by receiver function analysis: Implications for isostatic compensation. J. Geophys. Res. https://doi.org/10.1029/2001jb000422

Ault, A.K., Gautheron, C., King, G.E., 2019. Innovations in (U–Th)/He, Fission Track, and Trapped Charge Thermochronometry with Applications to Earthquakes, Weathering, Surface-Mantle Connections, and the Growth and Decay of Mountains. Tectonics. https://doi.org/10.1029/2018tc005312

Baby, G., Guillocheau, F., Morin, J., Ressouche, J., Robin, C., Broucke, O., Dall'Asta, M., 2018. Post-rift stratigraphic evolution of the Atlantic margin of Namibia and South Africa: Implications for the vertical movements of the margin and the uplift history of the South African Plateau. Marine and Petroleum Geology. https://doi.org/10.1016/j.marpetgeo.2018.06.030

Bernardes, R.B., Soares, J.E.P., Lima, M.V.A.G. de, Fuck, R.A., Viana, A.R., 2023. Cretaceous magmatic underplating and delamination beneath continental SE Brazil and their tectonic implications: Evidence from the PABBRISE wide-angle reflection and refraction seismic profile. Tectonophysics. https://doi.org/10.1016/j.tecto.2023.229856

Bertolini, G., Marques, J.C., Hartley, A.J., Da-Rosa, A.A.S., Scherer, C.M.S., Basei, M.A.S., Frantz, J.C., 2020. Controls on Early Cretaceous desert sediment provenance in south-west Gondwana, Botucatu Formation (Brazil and Uruguay). Sedimentology. https://doi.org/10.1111/sed.12715

Besser, M.L., Vasconcellos, E.M.G., Nardy, A.J.R., 2018. Morphology and stratigraphy of Serra Geral silicic lava flows in the northern segment of the Torres Trough, Paraná Igneous Province. Braz. J. Geol. https://doi.org/10.1590/2317-4889201820180087

Bicca, M.M., Kalkreuth, W., da Silva, T.F., de Oliveira, C.H.E., Genezini, F.A., 2020. Thermal and depositional history of Early-Permian Rio Bonito Formation of southern Paraná Basin – Brazil. International Journal of Coal Geology. https://doi.org/10.1016/j.coal.2020.103554

Bittencourt, A.C.S.P., Dominguez, J.M.L., Ussami, N., 1999. Flexure as a Tectonic Control on the Large Scale Geomorphic Characteristics of the Eastern Brazil Coastal Zone. Journal of Coastal Research.

Boldreel, L.O., Andersen, M.S., 1998. Tertiary compressional structures on the Faroe–Rockall Plateau in relation to northeast Atlantic ridge-push and Alpine foreland stresses. Tectonophysics. https://doi.org/10.1016/s0040-1951(98)00231-5

Braun, J., 2018. A review of numerical modeling studies of passive margin escarpments leading to a new analytical expression for the rate of escarpment migration velocity. Gondwana Research. https://doi.org/10.1016/j.gr.2017.04.012

Braun, J., van der Beek, P., 2004. Evolution of passive margin escarpments: What can we learn from low-temperature thermochronology? J. Geophys. Res. https://doi.org/10.1029/2004jf000147

Brosens, L., Cox, R., Campforts, B., Jacobs, L., Vanacker, V., Bierman, P., Razanamahandry, V.F., Rakotondrazafy, A.F.M., Razafimbelo, T., Rafolisy, T., Govers, G., 2023. The slow downwearing of Madagascar: Inferring patterns and controls on long-term basin-averaged erosion rates from in situ10Be at the catchment and regional level. Earth Surf Processes Landf. https://doi.org/10.1002/esp.5586

Brown, R.W., Summerfield, M.A., Gleadow, A.J.W., 2002. Denudational history along a transect across the Drakensberg Escarpment of southern Africa derived from apatite fission track thermochronology. J. Geophys. Res. https://doi.org/10.1029/2001jb000745

Canile, F.M., Babinski, M., Rocha-Campos, A.C., 2016. Evolution of the Carboniferous-Early Cretaceous units of Paraná Basin from provenance studies based on U-Pb, Hf and O isotopes from detrital zircons. Gondwana Research. https://doi.org/10.1016/j.gr.2016.08.008

Chaves, C., Ussami, N., Ritsema, J., 2016. Density and P-wave velocity structure beneath the Paraná Magmatic Province: Refertilization of an ancient lithospheric mantle. Geochem. Geophys. Geosyst. https://doi.org/10.1002/2016gc006369

Clark, S.R., 2018. Uncertainty in the breakup, spreading history, and velocity variations of Gondwana. Gondwana Research. https://doi.org/10.1016/j.gr.2017.04.029

Cobbold, P.R., Rossello, E.A., Roperch, P., Arriagada, C., Gómez, L.A., Lima, C., 2007. Distribution, timing, and causes of Andean deformation across South America. SP. https://doi.org/10.1144/gsl.sp.2007.272.01.174

Codilean, A.T., Fülöp, R.-H., Munack, H., Wilcken, K.M., Cohen, T.J., Rood, D.H., Fink, D., Bartley, R., Croke, J., Fifield, L.K., 2021. Controls on denudation along the East Australian continental margin. Earth-Science Reviews. https://doi.org/10.1016/j.earscirev.2021.103543

Cogné, N., Gallagher, K., Cobbold, P.R., 2011. Post-rift reactivation of the onshore margin of southeast Brazil: Evidence from apatite (U–Th)/He and fission-track data. Earth and Planetary Science Letters. https://doi.org/10.1016/j.epsl.2011.06.025

Cogné, N., Gallagher, K., Cobbold, P.R., Riccomini, C., Gautheron, C., 2012. Post-breakup tectonics in southeast Brazil from thermochronological data and combined inverse-forward thermal history modeling. J. Geophys. Res. https://doi.org/10.1029/2012jb009340

Colleps, C.L., McKenzie, N.R., Guenthner, W.R., Sharma, M., Gibson, T.M., Stockli, D.F., 2021. Apatite (U-Th)/He thermochronometric constraints on the northern extent of the Deccan large igneous province. Earth and Planetary Science Letters 571, 117087. https://doi.org/10.1016/j.epsl.2021.117087

Contreras, J., Zühlke, R., Bowman, S., Bechstädt, T., 2010. Seismic stratigraphy and subsidence analysis of the southern Brazilian margin (Campos, Santos and Pelotas basins). Marine and Petroleum Geology. https://doi.org/10.1016/j.marpetgeo.2010.06.007

Danišík, M., Kirkland, C.L., 2023. Thermochronometry constraints on south West Greenland passive continental margin development. Commun Earth Environ. https://doi.org/10.1038/s43247-023-00786-6

de Souza, D.H., Stuart, F.M., Rodés, Á., Pupim, F.N., Hackspacher, P.C., 2019. Controls on the erosion of the continental margin of southeast Brazil from cosmogenic 10Be in river sediments. Geomorphology. https://doi.org/10.1016/j.geomorph.2019.01.020

Donelick, R.A., 2005. Apatite Fission-Track Analysis. Reviews in Mineralogy and Geochemistry. https://doi.org/10.2138/rmg.2005.58.3

Evans, N.J., Byrne, J.P., Keegan, J.T., Dotter, L.E., 2005. Determination of Uranium and Thorium in Zircon, Apatite, and Fluorite: Application to Laser (U-Th)/He Thermochronology. J Anal Chem. https://doi.org/10.1007/s10809-005-0260-1

Flowers, R.M., Ketcham, R.A., Shuster, D.L., Farley, K.A., 2009. Apatite (U–Th)/He thermochronometry using a radiation damage accumulation and annealing model. Geochimica et Cosmochimica Acta. https://doi.org/10.1016/j.gca.2009.01.015

Fonseca, A., Novo, T., Fonte-Boa, T., Kuchenbecker, M., Fragoso, D.G.C., Peifer, D., Pedrosa-Soares, A.C., De Grave, J., 2023. Control of inherited structural fabric on the development and exhumation of passive margins – Insights from the Araçuaí Orogen (Brazil). Geoscience Frontiers 14, 101628. https://doi.org/10.1016/j.gsf.2023.101628

Fonte-Boa, T.M.R., Peifer, D., Fonseca, A., Novo, T.A., 2022. The southeast Brazilian rifted continental margin is not a single, continuous upwarp: Variations in morphology and denudation patterns along the continental drainage divide. Earth-Science Reviews. https://doi.org/10.1016/j.earscirev.2022.104091

Fraser, K.I., Enkelmann, E., Jess, S., Gilbert, H., Grieco, R., 2021. Resolving the Cenozoic History of Rock Exhumation Along the Central Rocky Mountain Trench Using Apatite Low-Temperature Thermochronology. Tectonics. https://doi.org/10.1029/2021tc006847

Frazer, W.D., Korenaga, J., 2022. Dynamic topography and the nature of deep thick plumes. Earth and Planetary Science Letters. https://doi.org/10.1016/j.epsl.2021.117286

Gallagher, K., 2012. Transdimensional inverse thermal history modeling for quantitative thermochronology. J. Geophys. Res. https://doi.org/10.1029/2011jb008825

Gallagher, K., Brown, R., Johnson, C., 1998. Fission Track Analysis And Its Applications To Geological Problems. Annu. Rev. Earth Planet. Sci. https://doi.org/10.1146/annurev.earth.26.1.519

Gallagher, K., Hawkesworth, C.J., Mantovani, M.S.M., 1994. The denudation history of the onshore continental margin of SE Brazil inferred from apatite fission track data. J. Geophys. Res. https://doi.org/10.1029/94jb00661

Gautheron, C., Tassan-Got, L., Ketcham, R.A., Dobson, K.J., 2012. Accounting for long alpha-particle stopping distances in (U–Th–Sm)/He geochronology: 3D modeling of diffusion, zoning, implantation, and abrasion. Geochimica et Cosmochimica Acta. https://doi.org/10.1016/j.gca.2012.08.016

Gerin, C., Gautheron, C., Oliviero, E., Bachelet, C., Mbongo Djimbi, D., Seydoux-Guillaume, A.-M., Tassan-Got, L., Sarda, P., Roques, J., Garrido, F., 2017. Influence of vacancy damage on He diffusion in apatite, investigated at atomic to mineralogical scales. Geochimica et Cosmochimica Acta 197, 87–103. https://doi.org/10.1016/j.gca.2016.10.018

Gernon, T.M., Hincks, T.K., Brune, S., Braun, J., Jones, S.M., Keir, D., Cunningham, A., Glerum, A., 2024. Coevolution of craton margins and interiors during continental break-up. Nature. https://doi.org/10.1038/s41586-024-07717-1

Gezatt, J.N., Macdonald, D.I.M., Stephenson, R., Jelinek, A.R., Carter, A., 2021. South Atlantic passive margin evolution: A thermochronology case study from the Rio de Janeiro-Três Rios section, SE Brazil. Journal of South American Earth Sciences. https://doi.org/10.1016/j.jsames.2020.103051

Gibson, S.A., Thompson, R.N., Leonardos, O.H., Dickin, A.P., Mitchell, J.G., 1999. The limited extent of plume-lithosphere interactions during continental flood-basalt genesis: geochemical evidence from Cretaceous magmatism in southern Brazil. Contributions to Mineralogy and Petrology. https://doi.org/10.1007/s004100050588

Gomes, A.S., Vasconcelos, P.M., 2021. Geochronology of the Paraná-Etendeka large igneous province. Earth-Science Reviews. https://doi.org/10.1016/j.earscirev.2021.103716

Gomes, M.C.V., Vieira, B.C., Salgado, A.A.R., Braucher, R., 2022. Debris flow and long-term denudation rates in a tropical passive margin escarpment in South America. Geomorphology. https://doi.org/10.1016/j.geomorph.2022.108333

Gonzalez, V.S, Bierman, P.R., Fernandes, N.F., Rood, D.H., 2016. Long-term background denudation rates of southern and southeastern Brazilian watersheds estimated with cosmogenic 10Be. Geomorphology. https://doi.org/10.1016/j.geomorph.2016.05.024

Green, P., Duddy, I., Japsen, P., 2022. Episodic kilometre-scale burial and exhumation and the importance of missing section. Earth-Science Reviews. https://doi.org/10.1016/j.earscirev.2022.104226

Griffis, N.P., Montañez, I.P., Mundil, R., Richey, J., Isbell, J., Fedorchuk, N., Linol, B., Iannuzzi, R., Vesely, F., Mottin, T., da Rosa, E., Keller, B., Yin, Q.-Z., 2019. Coupled stratigraphic and U-Pb zircon age constraints on the late Paleozoic icehouse-to-greenhouse turnover in south-central Gondwana. Geology. https://doi.org/10.1130/g46740.1

Gunnell, Y., Fleitout, L., 1998. Shoulder uplift of the Western Ghats passive margin, India: a denudational model. Earth Surf. Process. Landforms. https://doi.org/10.1002/(sici)1096-9837(199805)23:5<391::aid-esp853>3.0.co;2-5

Haag, M.B., Schoenbohm, L.M., Wolpert, J., Jess, S., Bierman, P., Corbett, L., Sommer, C.A., Endrizzi, G., 2025a. Rock strength controls erosion in tectonically dead landscapes. Sci. Adv. https://doi.org/10.1126/sciadv.adr2610

Haag, M.B., Schoenbohm, L.M., Jess, S., Bierman, P., Wolpert, J., Corbett, L., Sommer, C.A., 2025b. Erosional dynamics and escarpment retreat at the southern end of the South American passive margin escarpment. Geomorphology 486, 109885. https://doi.org/10.1016/j.geomorph.2025.109885

Hardenbol, J., Thierry, J., Farley, M.B., Jacquin, T.,De Graciansky, P.C., and Vail, P.R., 1998,Mesozoic and Cenozoic sequence chronostratigraphic framework of European basins: Society of Economic Paleontologists and Mineralogists Special Publication 60, p. 3–13.

Hasebe, N., Barbarand, J., Jarvis, K., Carter, A., Hurford, A.J., 2004. Apatite fission-track chronometry using laser ablation ICP-MS. Chemical Geology. https://doi.org/10.1016/j.chemgeo.2004.01.007

Hasebe, N., Tamura, A., Arai, S., 2013. Zeta equivalent fission-track dating using LA-ICP-MS and examples with simultaneous U–Pb dating. Island Arc. https://doi.org/10.1111/iar.12040

Hoggard, M.J., White, N., Al-Attar, D., 2016. Global dynamic topography observations reveal limited influence of large-scale mantle flow. Nature Geosci. https://doi.org/10.1038/ngeo2709

Horton, B.K., 2018. Tectonic Regimes of the Central and Southern Andes: Responses to Variations in Plate Coupling During Subduction. Tectonics 37, 402–429. https://doi.org/10.1002/2017tc004624

Hueck, M., Dunkl, I., Heller, B., Stipp Basei, M.A., Siegesmund, S., 2018. (U-Th)/He Thermochronology and Zircon Radiation Damage in the South American Passive Margin: Thermal Overprint of the Paraná LIP? Tectonics. https://doi.org/10.1029/2018tc005041

Hueck, M., Dunkl, I., Oriolo, S., Wemmer, K., Basei, M.A.S., Siegesmund, S., 2019. Comparing contiguous high- and low-elevation continental margins: New (U-Th)/He constraints from South Brazil and an integration of the thermochronological record of the southeastern passive margin of South America. Tectonophysics. https://doi.org/10.1016/j.tecto.2019.228222

Japsen, P., Chalmers, J.A., Green, P.F., Bonow, J.M., 2012. Elevated, passive continental margins: Not rift shoulders, but expressions of episodic, post-rift burial and exhumation. Global and Planetary Change. https://doi.org/10.1016/j.gloplacha.2011.05.004

Jean, A., Beauvais, A., Chardon, D., Arnaud, N., Jayananda, M., Mathe, P.E., 2019. Weathering history and landscape evolution of Western Ghats (India) from 40 Ar/ 39 Ar dating of supergene K–Mn oxides. JGS. https://doi.org/10.1144/jgs2019-048

Jess, S., Stephenson, R., Roberts, D.H., Brown, R., 2019. Differential erosion of a Mesozoic rift flank: Establishing the source of topography across Karrat, central West Greenland. Geomorphology. https://doi.org/10.1016/j.geomorph.2019.02.026

Jess, S., Stephenson, R., Roberts, D.H., Brown, R., 2020. Reply to: Thermal history solutions from thermochronology must be governed by geological relationships: A comment on Jess et al. (2019). Geomorphology. https://doi.org/10.1016/j.geomorph.2019.106971

Karl, M., Glasmacher, U.A., Kollenz, S., Franco-Magalhaes, A.O.B., Stockli, D.F., Hackspacher, P.C., 2013. Evolution of the South Atlantic passive continental margin in southern Brazil derived from zircon and apatite (U–Th–Sm)/He and fission-track data. Tectonophysics. https://doi.org/10.1016/j.tecto.2013.06.017

Ketcham, R.A., Gautheron, C., Tassan-Got, L., 2011. Accounting for long alpha-particle stopping distances in (U–Th–Sm)/He geochronology: Refinement of the baseline case. Geochimica et Cosmochimica Acta. https://doi.org/10.1016/j.gca.2011.10.011

Krob, F.C., Glasmacher, U.A., Bunge, H.-P., Friedrich, A.M., Hackspacher, P.C., 2020. Application of stratigraphic frameworks and thermochronological data on the Mesozoic SW Gondwana intraplate environment to retrieve the Paraná-Etendeka plume movement. Gondwana Research. https://doi.org/10.1016/j.gr.2020.02.010

Krob, F.C., Glasmacher, U.A., Karl, M., Perner, M., Hackspacher, P.C., Stockli, D.F., 2019. Multi-chronometer thermochronological modelling of the Late Neoproterozoic to recent t-T-evolution of the SE coastal region of Brazil. Journal of South American Earth Sciences. https://doi.org/10.1016/j.jsames.2019.02.012

Leroy, M., Gueydan, F., Dauteuil, O., 2008. Uplift and strength evolution of passive margins inferred from 2-D conductive modelling. Geophysical Journal International. https://doi.org/10.1111/j.1365-246x.2007.03566.x

Machado, J.P.S.L., Jelinek, A.R., Bicca, M.M., Stephenson, R., Genezini, F.A., 2019. West Gondwana orogenies and Pangaea break-up: thermotectonic effects on the southernmost Mantiqueira Province, Brazil. JGS. https://doi.org/10.1144/jgs2019-018

Machado, J.P.S.L., Jelinek, A.R., Stephenson, R., Gaucher, C., Müller Bicca, M., Chiglino, L., Genezini, F.A., 2020. Low-temperature thermochronology of the South Atlantic margin along Uruguay and its relation to tectonic events in West Gondwana. Tectonophysics. https://doi.org/10.1016/j.tecto.2020.228439

Maia, T.M., dos Santos, A.C., Rocha-Júnior, E.R.V., Valeriano, C. de M., Mendes, J.C., Jeck, I.K., dos Santos, W.H., de Oliveira, A.L., Mohriak, W.U., 2021. First petrologic data for Vitória Seamount, Vitória-Trindade Ridge, South Atlantic: a contribution to the Trindade mantle plume evolution. Journal of South American Earth Sciences. https://doi.org/10.1016/j.jsames.2021.103304

Makhubela, T.V., Kramers, J.D., Konyana, S.M., van Niekerk, H.S., Winkler, S.R., 2021. Erosion rates and weathering timescales in the eastern Great Escarpment, South Africa. Chemical Geology. https://doi.org/10.1016/j.chemgeo.2021.120368

Mariani, P., Braitenberg, C., Ussami, N., 2013. Explaining the thick crust in Paraná basin, Brazil, with satellite GOCE gravity observations. Journal of South American Earth Sciences. https://doi.org/10.1016/j.jsames.2013.03.008

McKay, R., Enkelmann, E., Hadlari, T., Matthews, W., Mouthereau, F., 2021. Cenozoic Exhumation History of the Eastern Margin of the Northern Canadian Cordillera. Tectonics. https://doi.org/10.1029/2020tc006582

Milani, E.J., de Melo, J.H.G., de Souza,P.A., Fernandes, L.A., França, A.B., 2007. Bacia do Paraná Bol. Geociencias Petrobras, 15 (2), pp. 265-287.

Mills, B.J.W., Krause, A.J., Scotese, C.R., Hill, D.J., Shields, G.A., Lenton, T.M., 2019. Modelling the long-term carbon cycle, atmospheric CO2, and Earth surface temperature from late Neoproterozoic to present day. Gondwana Research. https://doi.org/10.1016/j.gr.2018.12.001

Mosar, J., Lewis, G., Torsvik, TrondH., 2002. North Atlantic sea-floor spreading rates: implications for the Tertiary development of inversion structures of the Norwegian–Greenland Sea. JGS. https://doi.org/10.1144/0016-764901-135

Nielsen, S.B., Gallagher, K., Leighton, C., Balling, N., Svenningsen, L., Jacobsen, B.H., Thomsen, E., Nielsen, O.B., Heilmann-Clausen, C., Egholm, D.L., Summerfield, M.A., Clausen, O.R., Piotrowski, J.A., Thorsen, M.R., Huuse, M., Abrahamsen, N., King, C., Lykke-Andersen, H., 2009. The evolution of western Scandinavian topography: A review of Neogene uplift versus the ICE (isostasy–climate–erosion) hypothesis. Journal of Geodynamics. https://doi.org/10.1016/j.jog.2008.09.001

Nyblade, A.A., Sleep, N.H., 2003. Long lasting epeirogenic uplift from mantle plumes and the origin of the Southern African Plateau. Geochem Geophys Geosyst 4. https://doi.org/10.1029/2003gc000573

Riccomini, C., Peloggia, A.U.G., Saloni, J.C.L., Kohnke, M.W., Figueira, R.M., 1989. Neotectonic activity in the Serra do Mar rift system (southeastern Brazil). Journal of South American Earth Sciences. https://doi.org/10.1016/0895-9811(89)90046-1

Rohais, S., Lovecchio, J.P., Abreu, V., Miguez, M., Paulin, S., 2021. High-resolution sedimentary budget quantification – Example from the Cenozoic deposits in the Pelotas Basin, South Atlantic. Basin Research 33, 2252–2280. https://doi.org/10.1111/bre.12556

Rossetti, L., Lima, E.F., Waichel, B.L., Hole, M.J., Simões, M.S., Scherer, C.M.S., 2018. Lithostratigraphy and volcanology of the Serra Geral Group, Paraná-Etendeka Igneous Province in Southern Brazil: Towards a formal stratigraphical framework. Journal of Volcanology and Geothermal Research. https://doi.org/10.1016/j.jvolgeores.2017.05.008

Salgado, A.A.R., Marent, B.R., Cherem, L.F.S., Bourlès, D., Santos, L.J.C., Braucher, R., Barreto, H.N., 2013. Denudation and retreat of the Serra do Mar escarpment in southern Brazil derived from in situ-produced 10Be concentration in river sediment. Earth Surf Processes Landf. https://doi.org/10.1002/esp.3448

Salgado, A.A.R., Rezende, E. de A., Bourlès, D., Braucher, R., da Silva, J.R., Garcia, R.A., 2016. Relief evolution of the Continental Rift of Southeast Brazil revealed by in situ-produced 10Be concentrations in river-borne sediments. Journal of South American Earth Sciences. https://doi.org/10.1016/j.jsames.2016.02.002

Salomon, E., Koehn, D., Passchier, C., Hackspacher, P.C., Glasmacher, U.A., 2015. Contrasting stress fields on correlating margins of the South Atlantic. Gondwana Research. https://doi.org/10.1016/j.gr.2014.09.006

Scherer, C.M.S., 2000. Eolian dunes of the Botucatu Formation (Cretaceous) in southernmost Brazil: morphology and origin. Sedimentary Geology. https://doi.org/10.1016/s0037-0738(00)00135-4

Scherer, C.M.S., Reis, A.D., Horn, B.L.D., Bertolini, G., Lavina, E.L.C., Kifumbi, C., Goso Aguilar, C., 2023. The stratigraphic puzzle of the permo-mesozoic southwestern Gondwana: The Paraná Basin record in geotectonic and palaeoclimatic context. Earth-Science Reviews. https://doi.org/10.1016/j.earscirev.2023.104397

Steinberg, J., Gvirtzman, Z., Garfunkel, Z., 2014. Flexural response of a continental margin to sedimentary loading and lithospheric rupturing: The mountain ridge between the Levant Basin and the Dead Sea Transform. Tectonics. https://doi.org/10.1002/2013tc003330

Stica, J.M., Zalán, P.V., Ferrari, A.L., 2014. The evolution of rifting on the volcanic margin of the Pelotas Basin and the contextualization of the Paraná–Etendeka LIP in the separation of Gondwana in the South Atlantic. Marine and Petroleum Geology. https://doi.org/10.1016/j.marpetgeo.2013.10.015

Tassara, A., Swain, C., Hackney, R., Kirby, J., 2007. Elastic thickness structure of South America estimated using wavelets and satellite-derived gravity data. Earth and Planetary Science Letters. https://doi.org/10.1016/j.epsl.2006.10.008

Thompson, R.N., Gibson, S.A., Mitchell, J.G., Dickin, A.P., Leonardos, O.H., Brod, J.A., Greenwood, J.C., 1998. Migrating Cretaceous-Eocene Magmatismin the Serra do Mar Alkaline Province,SE Brazil: Melts from the Deflected Trindade Mantle Plume? Journal of Petrology. https://doi.org/10.1093/petroj/39.8.1493

Thybo, H., Artemieva, I.M., 2013. Moho and magmatic underplating in continental lithosphere. Tectonophysics. https://doi.org/10.1016/j.tecto.2013.05.032

van der Beek, P., Summerfield, M.A., Braun, J., Brown, R.W., Fleming, A., 2002. Modeling postbreakup landscape development and denudational history across the southeast African (Drakensberg Escarpment) margin. J. Geophys. Res. https://doi.org/10.1029/2001jb000744

Van Ranst, G., Pedrosa-Soares, A.C., Novo, T., Vermeesch, P., De Grave, J., 2020. New insights from low-temperature thermochronology into the tectonic and geomorphologic evolution of the south-eastern Brazilian highlands and passive margin. Geoscience Frontiers. https://doi.org/10.1016/j.gsf.2019.05.011

Veizer, J., Ala, D., Azmy, K., Bruckschen, P., Buhl, D., Bruhn, F., Carden, G.A.F., Diener, A., Ebneth, S., Godderis, Y., Jasper, T., Korte, C., Pawellek, F., Podlaha, O.G., Strauss, H., 1999. 87Sr/86Sr, δ13C and δ18O evolution of Phanerozoic seawater. Chemical Geology. https://doi.org/10.1016/s0009-2541(99)00081-9

Vieira, F., Hamza, V., 2019. Assessment of Geothermal Resources of South America - A New Look. ijthfa. https://doi.org/10.31214/ijthfa.v2i1.32

Wang, Y., Willett, S.D., 2021. Escarpment retreat rates derived from detrital cosmogenic nuclide concentrations. Earth Surf. Dynam. https://doi.org/10.5194/esurf-9-1301-2021

Wang, Y., Willett, S.D., Wu, D., Haghipour, N., Christl, M., 2021. Retreat of the Great Escarpment of Madagascar From Geomorphic Analysis and Cosmogenic 10Be Concentrations. Geochem Geophys Geosyst. https://doi.org/10.1029/2021gc009979

Weissel, J.K., Seidl, M.A., 1998. Inland propagation of erosional escarpments and river profile evolution across the southeast Australian passive continental margin. Geophysical Monograph Series. https://doi.org/10.1029/gm107p0189

Wildner, W., Camozzato, E., Toniolo, J.A., Binotto, R.B., Iglesias,C.M.F., Laux, J. H., 2014. Mapa geológico do estado de Santa Catarina (Technical Report, Geological Survey of Brazil, 2014); https://rigeo.cprm.gov.br/jspui/handle/doc/17996.

Wildner, W., Ramgrab, G.E., Lopes, R.C., Iglesias, C.M.F., 2008. Geologia e recursos minerais do estado do Rio Grande do Sul (Technical Report, Geological Survey of Brazil); https://rigeo.sgb.gov.br/handle/doc/10301.

Wygrala, B. P., 1989, Integrated study of an oil field in the Southern Po-basin, Northern Italy (Ph. D. Thesis): University of Köln. (Ber. Forschungszentrum Jülich 2313, 217 pp.)

Supplementary Information 1 – Field aspects and sampling sites

Fig. S1.1 – (A-B) Field aspects of the study area in the Aparados da Serra region and (C-F) representative sampling sites near the lava-sediment contact. Black boxes are placed in (C) to cover people. **Sampling locations (lat, long) are reported in Table S7.2**.

Supplementary Information 2 – Mineral separation

Initially, rock fragments were disaggregated by repeatedly passing them through a jaw crusher. Because of the low-strength and weak diagenesis of the sampled units, this first step was usually effective in producing enough sand-sized material (< 300 μm), which allowed us to avoid the use of mills and potentially preserve a higher amount of whole apatites for the (U-Th-Sm)/He analysis (Donelick et al., 2005).

To remove the dust and the clay fraction, samples were repeatedly washed with tap water in a bucket until the water attained clarity and later dried at room temperature (ca. 21 °C) for two weeks. Finally, the dried material was sieved in six categories: (i) > 500μm, (ii) 500 - 250 μm, (iii) 250 - 125 μm, (iv) 25 - 63 μm, and (vi) < 63 μm. Categories i, ii, and vi generally accounted for < 15% of the total sample mass and were excluded from further processing.

Following sieving, the silty/sandy fraction (250 - 63 μm) was submitted to vertical magnetic separation to remove strongly magnetic minerals (e.g., magnetite, hematite). This was accomplished using a Frantz isodynamic magnetic separator model, with increasing field strengths of 0.5, 1.0, and 1.5 A, where only the non-magnetic fraction was kept and further processed.

Density separation was achieved using a concentrated solution of lithium heteropolytungstates (LST, density = 2.95 g/mL), resulting in a heavy fraction that included apatite, zircon, tourmaline, and other common heavy minerals. The heavy fraction was submitted to a second separation step using Methylene Iodide (MI, density = 3.32 g/mL), from which only the light fraction was kept. At this stage, most samples had been reduced to ∼ 20g. Lastly, we submit the heavy LST/light MI fraction to horizontal magnetic separation using a Frantz isodynamic magnetic separator set to a tilt of 5° and a slope of 10°.

Supplementary Information 3 – AHe data

Table 3.1 – AHe grain characterization, alpha correction and analytical results. W = width, L = length, H = height.

Sample	Grain geometry				Grain composition						Ft correction			Uncorr. Age (Ma) ± 2σ (abs)			Corr. Age (Ma) (abs)		± 2σ
	Grain	W (µm)	L (µm)	H (µm)	He (fmol/ug)	U (ppm)	Th (ppm)	Sm (ppm)	eU (ppm)	Th/U ratio	r' (µm)	Mass (µm)	Ft						
154-1 (BR-9)	a	87.3	71.1	147.8	10.52	8.28	82.37	170.22	28.09	9.94	43.3	1.50	0.66	69.4	±	3.3	**105.9**	±	5.1
	b	99.7	88.0	140.5	30.95	77.21	59.88	423.64	91.97	0.78	46.8	1.73	0.70	62.2	±	2.3	**88.3**	±	3.3
	c	82.5	69.4	141.7	60.50	173.96	93.11	400.24	196.60	0.54	41.5	1.31	0.67	56.9	±	1.9	**84.9**	±	2.9
	d	78.9	77.5	104.1	11.31	24.38	80.03	617.64	44.17	3.28	36.2	0.79	0.61	47.5	±	2.4	**77.9**	±	3.9
	e	75.0	65.5	133.4	6.52	10.06	45.87	152.40	21.16	4.56	38.5	1.06	0.63	57.0	±	2.8	**91.2**	±	4.6
154-2 (BR-10)	a	69.4	60.6	109.7	0.74	1.83	11.02	228.87	4.72	6.03	34.1	0.70	0.58	28.9	±	4.9	**50.0**	±	8.4
	b	66.2	60.6	123.8	2.33	9.00	33.23	95.39	17.02	3.69	34.8	0.80	0.59	25.4	±	3.8	**42.8**	±	6.3
	c	78.7	67.7	90.4	26.35	58.60	224.69	591.20	112.78	3.83	32.6	0.58	0.57	43.3	±	1.7	**76.4**	±	3.0
	d	74.9	72.8	104.6	3.56	11.66	20.90	333.67	17.03	1.79	35.4	0.75	0.61	38.7	±	4.6	**63.5**	±	7.5
	e	68.4	66.2	127.8	3.45	10.04	48.24	120.34	21.67	4.80	36.3	0.91	0.61	29.5	±	1.6	**48.8**	±	2.7
154-5 (BR-6)	a	82.2	78.4	114.2	3.14	11.18	35.77	347.55	20.12	3.20	38.7	0.97	0.63	29.0	±	1.6	**45.8**	±	2.5
	b	73.2	63.4	126.0	16.69	19.71	45.58	215.28	30.81	2.31	37.1	0.93	0.62	99.9	±	4.4	**160.7**	±	7.1
	c	96.3	90.0	128.3	6.57	28.84	46.57	319.45	40.31	1.61	44.2	1.44	0.68	30.2	±	1.4	**44.3**	±	2.0
	d	82.1	82.1	105.8	3.03	12.08	18.78	34.32	16.59	1.55	37.1	0.86	0.63	33.8	±	2.4	**54.0**	±	3.8
	e	62.1	61.3	147.3	5.05	6.05	57.56	513.85	20.36	9.52	35.2	0.96	0.58	46.0	±	2.9	**78.9**	±	5.0
154-8 (BR-7)	a	99.0	88.0	130.7	2.88	7.41	15.92	489.07	11.78	2.15	45.0	1.51	0.68	45.2	±	2.8	**66.1**	±	4.1
	b	80.1	78.9	134.3	3.39	10.55	11.03	286.15	13.51	1.05	41.1	1.24	0.66	46.5	±	4.0	**70.0**	±	6.0
	~~c*~~	~~76.7~~	~~74.9~~	~~107.5~~	~~37.70~~	~~2.33~~	~~12.60~~	~~135.25~~	~~5.49~~	~~5.40~~	~~36.3~~	~~0.81~~	~~0.60~~	~~1176.8~~	±	~~103.0~~	~~**-**~~	±	~~-~~
	d	62.9	65.5	126.0	3.66	12.06	9.53	338.47	14.73	0.79	34.5	0.80	0.61	45.9	±	5.2	**75.5**	±	8.6
	e	67.4	59.4	108.1	0.67	3.04	13.79	262.87	6.64	4.54	33.4	0.66	0.58	18.7	±	7.1	**32.5**	±	12.4
154-9 (BR-8)	a	71.5	65.9	86.1	0.37	1.44	5.04	6.71	2.65	3.49	36.5	1.49	0.60	26.1	±	3.5	**43.3**	±	5.7
	b	76.6	66.8	111.2	5.39	8.50	19.53	168.15	13.35	2.30	37.6	1.09	0.68	74.6	±	5.2	**110.5**	±	7.7
	c	70.2	63.6	107.1	2.02	12.58	42.20	143.46	22.79	3.36	34.3	0.70	0.59	16.5	±	0.7	**28.0**	±	1.2
	d	87.1	74.1	98.5	0.77	4.98	17.00	64.50	9.10	3.42	42.5	1.06	0.65	15.8	±	1.4	**24.4**	±	2.1
	e*	93.0	79.5	120.7	68.32	60.81	18.26	1326.36	66.75	0.30	43.8	1.68	0.74	186.8	±	6.4	**254.2**	±	8.7
	f	90.1	81.9	112.3	0.55	1.40	8.05	30.94	3.35	5.76	46.3	1.38	0.67	30.6	±	5.0	**45.8**	±	7.5
	g	68.8	59.3	86.1	5.61	11.32	58.35	242.90	25.50	5.15	32.0	0.65	0.62	40.8	±	2.7	**65.6**	±	4.4
154-10 (BR-5)	a	81.6	72.2	94.5	3.86	11.33	34.54	201.49	19.79	3.05	34.1	0.66	0.59	36.2	±	4.3	**61.5**	±	7.3
	b	86.1	69.6	116.9	4.41	27.05	1.66	40.65	27.49	0.06	39.0	1.00	0.66	29.7	±	2.8	**45.3**	±	4.3
	c	101.9	92.6	113.3	7.24	11.35	36.41	377.12	20.47	3.21	50.8	1.79	0.70	65.5	±	3.4	**93.1**	±	4.9
	d	84.8	72.0	118.3	4.42	7.19	39.56	130.36	16.76	5.50	40.9	1.39	0.69	48.8	±	2.4	**70.8**	±	3.5
	e	73.6	63.1	97.5	23.81	25.13	52.71	320.42	38.06	2.10	33.3	0.62	0.59	115.2	±	5.1	**197.0**	±	8.7
154-14 (BR-3)	a	73.5	67.8	100.4	3.38	9.30	1.26	278.51	9.93	0.14	34.1	0.67	0.61	62.8	±	10.9	**102.5**	±	17.8
	b	89.7	85.1	94.2	33.77	54.21	86.60	183.40	75.04	1.60	44.7	1.20	0.67	83.1	±	2.7	**124.0**	±	4.1
	c	79.0	75.4	149.1	9.82	29.71	25.49	137.40	35.95	0.86	42.0	1.41	0.67	50.5	±	2.5	**75.2**	±	3.7
	d	85.3	82.8	99.3	7.27	16.38	19.46	355.90	21.44	1.19	35.9	0.78	0.62	62.7	±	8.1	**101.5**	±	13.1

	e	86.8	81.8	90.7	6.81	11.13	3.93	30.53	12.10	0.35	43.1	1.08	0.67	103.5	±	5.6	**154.2**	±	8.3
154-15 (BR-4)	a	103.7	95.6	110.1	6.44	12.90	1.06	170.38	13.36	0.08	51.3	1.82	0.73	88.7	±	6.1	**122.3**	±	8.4
	b	76.6	72.1	113.9	14.81	33.25	15.54	366.91	37.39	0.47	37.2	0.88	0.64	73.1	±	6.0	**114.8**	±	9.4
	c	91.7	74.9	128.9	11.44	26.46	5.42	386.57	28.21	0.20	42.3	1.29	0.68	74.8	±	3.7	**109.8**	±	5.5
	d*	100.5	89.0	115.6	6.98	22.32	360.63	160.31	108.34	16.16	50.1	1.73	0.68	12.0	±	0.5	**17.6**	±	0.8
	e	65.7	63.8	128.8	2.75	11.93	7.12	51.98	13.69	0.60	35.4	0.86	0.62	37.2	±	4.8	**60.1**	±	7.8
154-16 (BR-2)	a	94.7	89.8	113.0	8.80	20.88	39.78	76.52	30.43	1.91	40.6	1.12	0.65	53.5	±	2.4	**81.8**	±	3.7
	b	100.6	88.1	125.0	17.29	32.93	29.71	92.72	40.11	0.90	50.9	1.85	0.72	79.5	±	2.4	**111.1**	±	3.4
	c	99.5	92.0	140.0	15.93	38.49	22.89	119.18	44.08	0.59	47.0	1.74	0.71	66.7	±	2.6	**94.4**	±	3.7
	d	99.2	91.5	136.2	16.94	28.69	23.19	62.54	34.29	0.81	46.2	1.66	0.70	91.0	±	2.8	**130.1**	±	4.0
	e	101.6	89.6	106.9	23.42	49.27	24.72	88.17	55.25	0.50	49.3	1.63	0.71	78.2	±	3.8	**110.1**	±	5.3
154-17 (BR-1)	a	85.4	73.3	148.1	20.73	32.41	57.73	280.80	46.49	1.78	43.9	1.86	0.71	82.3	±	2.8	**115.3**	±	4.0
	b	93.4	91.7	103.6	17.81	37.21	3.97	658.12	38.95	0.11	47.9	1.49	0.70	84.2	±	3.7	**120.3**	±	5.3
	c	80.7	71.7	112.1	4.66	8.62	6.99	31.65	10.33	0.81	37.6	0.90	0.64	83.2	±	8.7	**130.7**	±	13.6
	d	85.0	78.1	98.6	5.34	15.19	7.03	152.57	17.04	0.46	43.1	1.09	0.67	57.9	±	2.8	**86.5**	±	4.2
	e	69.6	68.6	103.1	22.96	86.44	35.65	165.52	95.13	0.41	33.9	0.67	0.61	44.7	±	1.6	**73.6**	±	2.6

Notes: eU: effective Uranium concentration; r: equivalent spherical radius; Ft: alpha correction factor, based on Ketcham et al. (2011).

* Excluded from modeling due to anomalous Sm or Th composition.

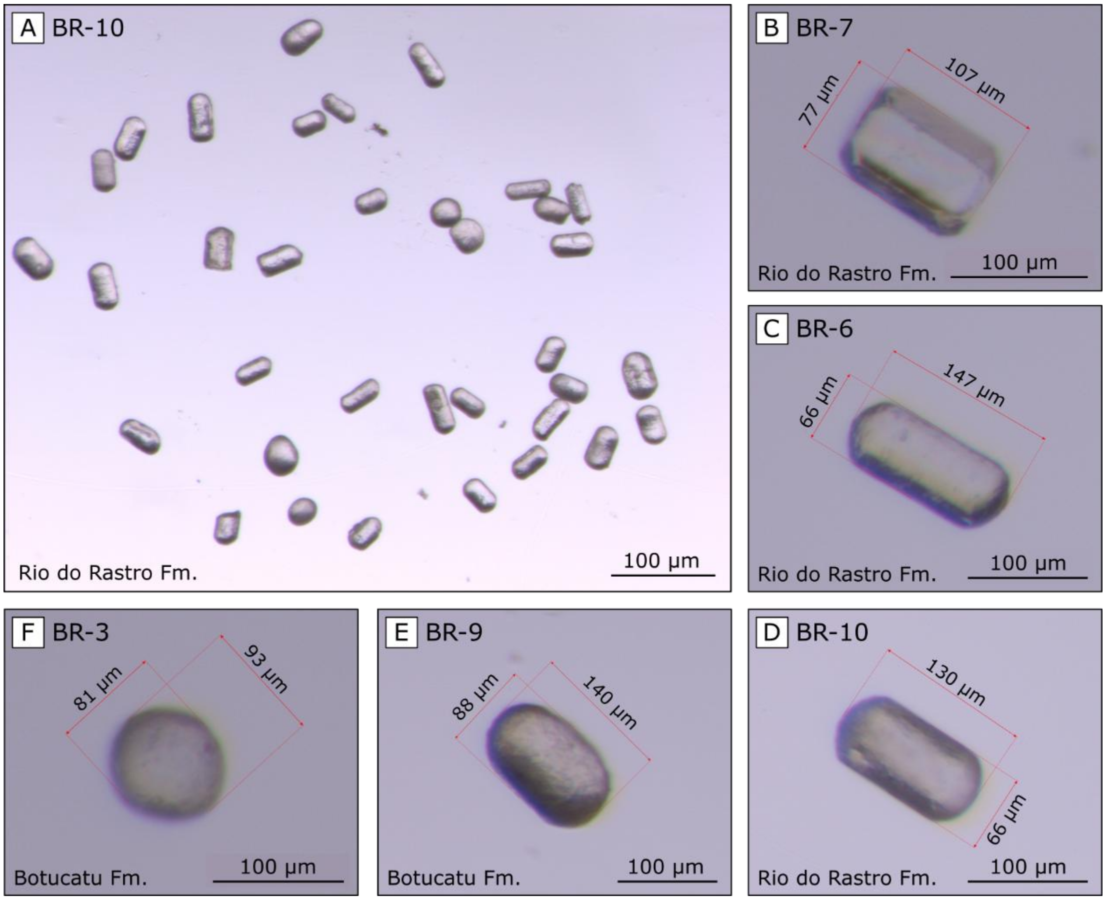

Fig. S3.2 – Stereomicroscope images displaying apatite diversity in the sampled units. A) Apatite separates in the Rio do Rastro Fm. B-F) Varying degrees of apatite abrasion across different samples. Apatites from the Rio do Rastro Fm. (B-D) tend to show less abrasion, while those from the Botucatu Fm. (E-F) are generally circular.

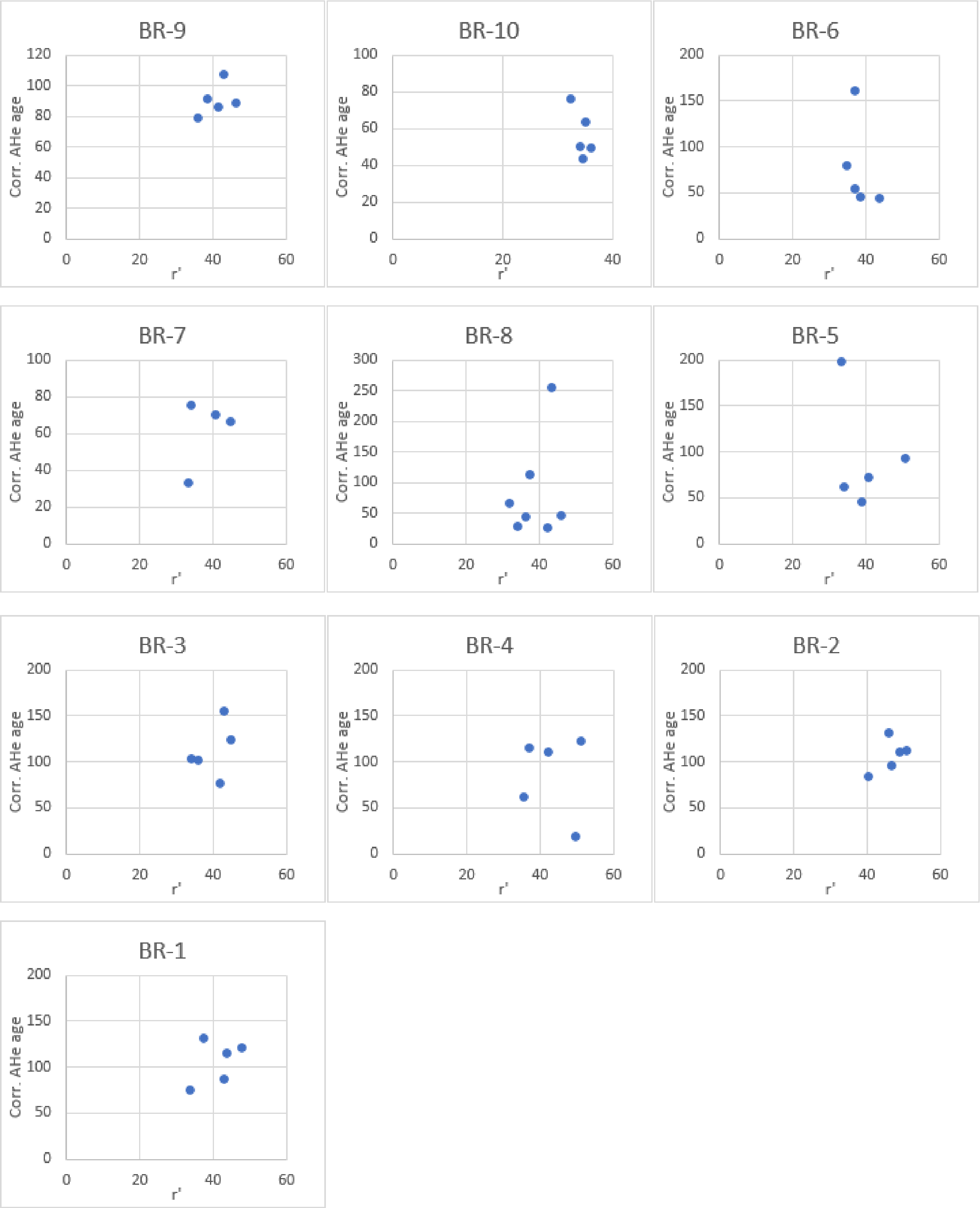

Fig. S3.3 – Equivalent radius (r’, in µm) versus corrected AHe age (Ma).

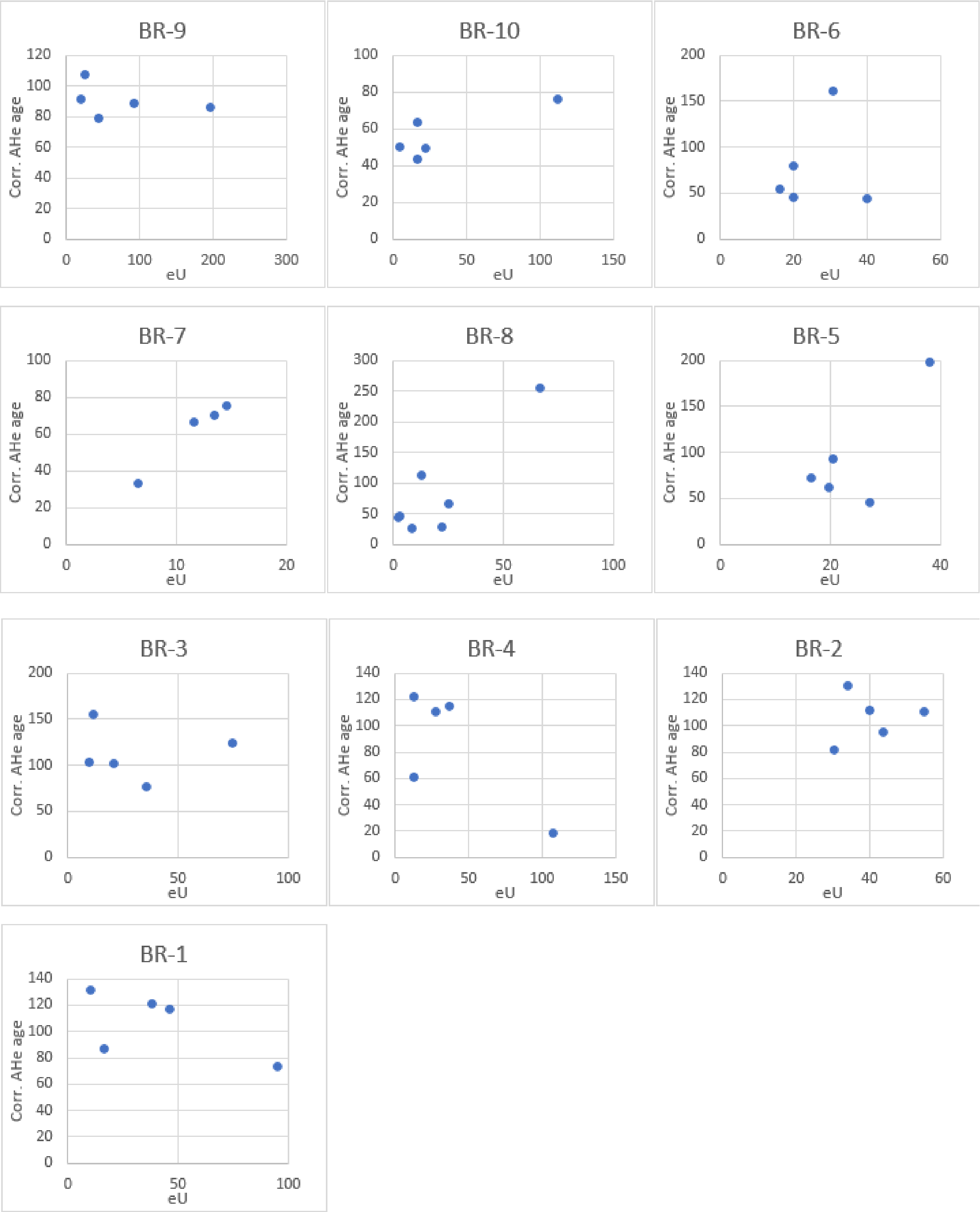

Fig. S3.4 – Effective uranium (eU, in ppm) versus corrected AHe age (Ma).

Supplementary Information 4 – AFT data

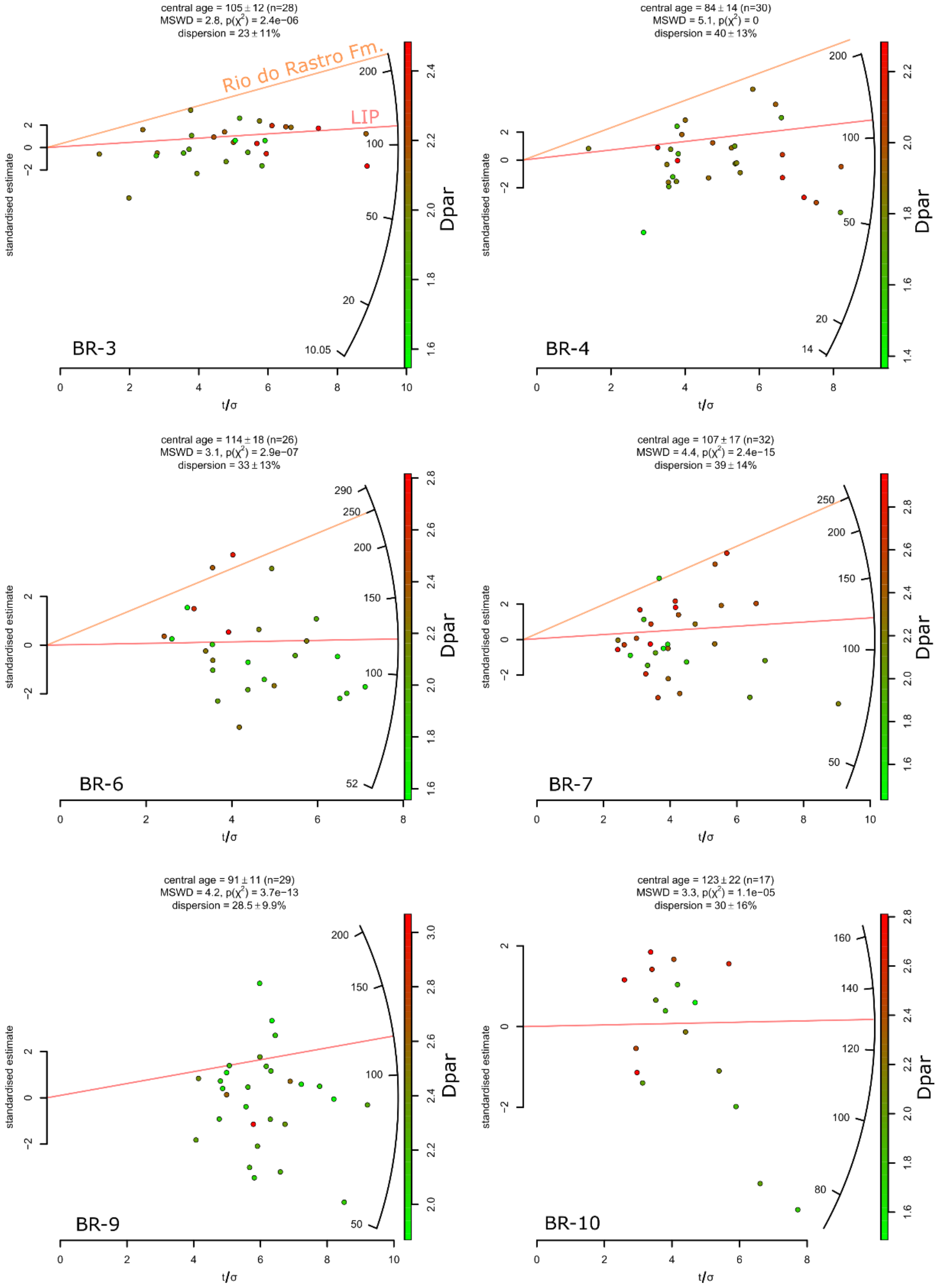

Fig. S4.1 – Radial plots displaying apatite fission track age distribution and histograms showing confined track lengths distributions. n: number of measurements.

Table S4.2 – Apatite confined fission track length data and diameter of track opening measured parallel to the crystallographic c-axis (Dpar).

Sample BR-3

Final length (μm)	Angle to c-axis	Projected length (μm)	Dpar (μm)	Dpar stdv (μm)
13.79	85.0	15.11	2.45	0.11
10.57	55.6	12.72	2.45	0.11
9.69	21.6	10.71	2.36	0.16
5.78	68.0	11.62	2.36	0.16
11.20	80.5	13.5	1.88	0.25
7.81	55.5	11.68	1.86	0.13
8.22	34.1	10.73	2.31	0.15
9.73	56.4	12.2	1.79	0.20
12.37	76.9	14.2	1.79	0.20
12.46	85.4	14.3	2.45	0.45
12.43	72.1	14.19	2.45	0.45
14.25	29.6	14.69	2.45	0.45
11.61	18.5	12.1	2.45	0.45
14.95	33.3	15.34	2.45	0.45
10.06	33.0	11.57	2.45	0.45
11.69	65.9	13.65	2.45	0.45
10.69	67.4	13.04	2.45	0.45
11.68	61.7	13.57	2.09	0.35
13.54	85.6	14.96	2.07	0.33
13.74	57.3	14.85	2.07	0.33
11.73	42.8	13.13	2.07	0.33
11.54	75.8	13.67	2.18	0.12
13.52	33.2	14.19	2.18	0.12
13.89	78.9	15.15	2.18	0.12
11.75	84.4	13.86	1.58	0.20
8.59	52.6	11.71	1.58	0.20
9.03	30.8	10.75	1.88	0.14
11.04	45.7	12.75	1.83	0.23
11.93	31.8	12.9	2.22	0.17
15.06	27.1	15.33	1.84	0.14
13.91	62.5	15.03	1.84	0.14
10.08	80.9	12.82	1.98	0.25

Sample BR-4

Final length (μm)	Angle to c-axis	Projected length (μm)	Dpar (μm)	Dpar stdv (μm)
14.09	45.2	14.89	1.80	0.27
11.72	57.9	13.52	2.00	0.11

10.56	64.1	12.9	2.00	0.11
14.45	51.7	15.25	2.00	0.11
11.93	80.6	13.95	2.16	0.23
12.42	68.9	14.15	1.69	0.38
12.43	39.8	13.54	2.01	0.10
13.09	59.7	14.45	2.01	0.10
13.42	27.4	13.95	2.01	0.10
11.22	64.9	13.33	2.01	0.10
12.93	67.2	14.45	1.73	0.29
14.61	55.1	15.41	1.73	0.29

Sample BR-6

Final length (μm)	Angle to c-axis	Projected length (μm)	Dpar (μm)	Dpar stdv (μm)
12.88	76.7	14.51	1.87	0.10
14.58	12.1	14.66	2.14	0.16
12.87	49.3	14.1	2.16	0.27
13.06	33.1	13.82	2.16	0.27
12.13	66.8	13.94	1.99	0.12
15.38	54.4	15.93	1.82	0.19
13.82	68.2	15.03	2.51	0.25
13.83	64.4	15	1.92	0.13
14.08	65.3	15.17	1.92	0.13
12.60	71.7	14.29	1.92	0.13
12.41	53.5	13.88	1.86	0.20
14.14	36.6	14.75	1.86	0.20
12.80	73.0	14.43	3.26	0.08
15.75	27.9	15.94	2.06	0.13
9.82	38.8	11.66	2.06	0.13
13.99	42.0	14.75	2.11	0.26
12.58	86.2	14.37	2.11	0.26
12.64	69.7	14.3	2.22	0.30
12.15	66.9	13.95	2.22	0.30
12.09	65.1	13.89	2.22	0.30
11.95	74.3	13.92	2.35	0.36
14.85	51.0	15.52	2.35	0.36
10.64	60.2	12.87	2.35	0.36
12.56	69.0	14.24	2.17	0.15
14.44	44.2	15.13	2.17	0.15
11.36	67.1	13.45	2.17	0.15
12.97	48.2	14.15	2.17	0.15
11.89	79.7	13.92	2.17	0.15
11.39	62.6	13.4	2.17	0.15
14.09	80.3	15.28	2.96	0.20

10.03	84.1	12.85	2.28	0.44
15.66	50.0	16.09	2.28	0.44
12.95	72.7	14.52	2.28	0.44
15.87	38.1	16.14	2.28	0.44
13.12	68.9	14.6	3.24	0.13
15.89	69.7	16.36	3.24	0.13
12.58	68.9	14.25	3.24	0.13
15.16	54.2	15.77	2.16	0.51
12.59	26.1	13.22	2.72	0.07
11.78	47.5	13.31	2.72	0.07
9.56	64.5	12.29	2.72	0.07
13.79	86.5	15.12	2.52	0.48
12.99	76.5	14.58	1.92	0.21
13.74	86.2	15.08	2.02	0.16
12.37	73.8	14.17	2.02	0.16
11.93	80.4	13.95	2.18	0.22
13.04	57.4	14.38	2.82	0.11
14.00	49.9	14.91	2.70	0.15
14.92	28.9	15.24	2.70	0.15
14.75	62.4	15.58	1.71	0.12
12.78	37.6	13.74	1.78	0.18
13.22	77.8	14.73	2.96	0.15
12.74	89.5	14.47	1.85	0.12
13.43	53.8	14.58	2.50	0.03
13.28	61.1	14.6	2.67	0.08
13.14	73.9	14.66	2.67	0.08
10.06	70.0	12.68	2.67	0.08
10.84	65.8	13.1	2.67	0.08
13.97	36.1	14.61	3.15	0.21
12.18	55.9	13.78	1.94	0.15
13.79	62.8	14.95	1.94	0.15
15.72	24.3	15.88	2.52	0.17
15.39	88.0	16.1	2.52	0.17
14.92	80.1	15.79	2.52	0.17
10.34	71.4	12.88	2.52	0.17
13.07	55.1	14.36	2.34	0.13
13.44	67.5	14.78	2.34	0.13
12.90	48.0	14.1	1.95	0.21
13.82	24.9	14.22	2.09	0.29
11.32	85.8	13.6	2.09	0.29
14.65	75.9	15.61	2.09	0.29
13.52	33.5	14.19	1.84	0.16
14.41	53.6	15.25	1.84	0.16
12.52	37.8	13.55	1.84	0.16
13.99	34.0	14.58	1.99	0.24

13.82	68.9	15.04	2.20	0.11
11.28	41.1	12.76	2.20	0.11
12.82	36.6	13.74	2.20	0.11
13.62	80.0	14.99	1.90	0.27
10.80	76.5	13.22	2.55	0.33
12.14	89.6	14.11	2.55	0.33
13.15	22.5	13.58	2.55	0.33
12.62	60.6	14.16	3.37	0.16
13.93	79.5	15.18	3.97	0.05
15.56	53.3	16.04	2.79	0.12
7.18	83.9	12.18	2.79	0.12
11.60	35.2	12.78	2.79	0.12
14.47	60.1	15.37	2.05	0.11
12.21	78.4	14.11	2.47	0.10
9.98	60.0	12.45	2.47	0.10
10.08	77.0	12.78	1.74	0.00
12.70	83.4	14.44	2.92	0.26
6.54	29.4	10.24	1.70	0.10
9.95	86.2	12.85	1.70	0.10
10.93	26.8	11.92	1.71	0.12

Sample BR-7

Final length (µm)	Angle to c-axis	Projected length (µm)	Dpar (µm)	Dpar stdv (µm)
13.90	37.1	14.58	2.03	0.36
12.30	54.3	13.83	2.69	0.14
11.05	65.7	13.24	2.69	0.14
10.33	71.3	12.87	2.04	0.22
11.35	58.1	13.28	2.04	0.22
12.10	65.0	13.89	2.79	0.22
12.63	84.6	14.4	2.54	0.28
12.29	73.0	14.11	2.70	0.20
12.93	84.9	14.58	2.19	0.20
13.13	77.6	14.67	3.16	0.14
10.86	43.6	12.55	2.20	0.24
13.72	85.8	15.07	2.76	0.14
8.50	30.6	10.51	2.54	0.40
13.22	79.1	14.74	2.54	0.40
14.30	68.0	15.34	2.15	0.41
11.39	63.7	13.42	2.15	0.41
13.79	67.9	15.01	2.53	0.50
14.93	32.7	15.31	2.79	0.16
14.31	31.0	14.77	2.79	0.16
12.78	54.8	14.16	1.86	0.43

14.02	69.5	15.17	2.33	0.13
12.11	71.4	13.98	2.33	0.13
15.91	58.6	16.33	3.26	0.45
13.27	49.3	14.38	3.26	0.45
12.91	61.2	14.36	3.26	0.45
16.17	46.1	16.43	3.44	0.24
14.12	86.8	15.32	2.11	0.30
12.37	67.9	14.11	2.11	0.30
9.29	88.8	12.69	2.98	0.21
9.20	83.1	12.61	2.98	0.21
12.85	62.9	14.34	3.16	0.51
14.58	62.9	15.47	3.16	0.51
15.23	63.4	15.9	2.97	0.31
10.88	63.9	13.1	2.40	0.42
13.48	47.4	14.49	2.80	0.24
12.34	46.3	13.66	3.30	0.20
13.09	59.4	14.45	3.30	0.20
13.66	43.4	14.54	2.30	0.17
14.26	30.3	14.72	2.24	0.14
12.94	65.5	14.44	2.24	0.14
12.79	44.6	13.94	2.24	0.14
12.17	82.5	14.11	3.22	0.10
12.46	65.8	14.14	3.15	0.11
14.69	48.0	15.37	2.56	0.17
14.23	57.4	15.18	2.58	0.37
13.34	80.8	14.82	2.95	0.51
13.48	45.8	14.46	2.44	0.40
13.69	27.6	14.18	2.44	0.40
13.21	75.1	14.71	2.44	0.40
13.43	70.4	14.8	2.44	0.40
15.05	43.5	15.57	3.36	0.53
14.88	87.8	15.78	3.36	0.53
11.54	59.1	13.43	2.80	0.21
13.71	73.8	15.01	2.80	0.21

Sample BR-9

Final length (µm)	Angle to c-axis	Projected length (µm)	Dpar (µm)	Dpar stdv (µm)
13.49	61.0	14.73	2.21	0.16
12.16	75.3	14.05	3.02	0.28
9.23	84.4	12.63	2.08	0.14
14.34	90.0	15.45	2.38	0.09
15.26	43.8	15.73	2.09	0.12
7.28	72.7	12.03	2.09	0.12

11.14	67.8	13.33	2.24	0.06
11.86	86.1	13.93	2.20	0.16
12.27	64.6	14	2.20	0.16
14.74	20.7	14.95	2.20	0.16
14.83	19.3	15	2.26	0.11
14.86	42.7	15.41	2.31	0.24
10.35	59.3	12.66	2.31	0.24
10.85	79.0	13.27	2.29	0.24
13.58	58.7	14.76	2.29	0.24
13.22	47.4	14.31	1.92	0.31
13.55	60.0	14.76	1.92	0.31
14.43	55.8	15.29	2.08	0.12
13.39	61.6	14.68	2.08	0.12
13.30	52.0	14.46	2.08	0.12
12.60	73.5	14.32	2.20	0.06
13.77	83.3	15.1	1.92	0.45
12.11	58.7	13.79	2.27	0.12
12.07	59.5	13.78	2.02	0.34
11.96	54.2	13.6	2.29	0.35
11.43	77.8	13.62	2.32	0.21
13.92	65.1	15.06	2.32	0.21
14.61	50.2	15.34	2.43	0.32
12.83	50.3	14.1	2.07	0.09
12.33	73.0	14.14	2.13	0.31
11.68	70.7	13.71	2.13	0.31
8.13	59.8	11.87	1.83	0.11
12.33	65.9	14.05	2.30	0.18
12.18	36.0	13.24	2.13	0.08
11.30	79.7	13.56	2.13	0.08
14.43	65.0	15.39	2.30	0.35
13.10	49.2	14.26	2.25	0.20
10.83	89.0	13.3	2.22	0.41
13.74	42.6	14.58	2.22	0.41
14.28	67.6	15.32	2.27	0.23
13.39	77.9	14.84	2.11	0.31
12.41	44.7	13.67	2.36	0.27
13.56	52.2	14.64	2.45	0.31
10.81	64.5	13.06	2.27	0.12
13.40	42.1	14.32	2.27	0.12
11.53	61.9	13.48	2.16	0.20

Sample BR-10

Final length (μm)	Angle to c-axis	Projected length (μm)	Dpar (μm)	Dpar stdv (μm)

10.60	50.5	12.6	2.10	0.34
10.48	76.2	13.02	2.14	0.23
12.59	52.1	13.98	1.99	0.13
12.42	53.1	13.88	1.86	0.14
12.02	52.9	13.61	1.78	0.07
13.63	72.6	14.95	1.86	0.09
10.18	55.5	12.47	2.13	0.25
12.84	82.2	14.52	2.13	0.25
10.84	53.8	12.85	2.13	0.25
14.54	34.0	15.02	2.09	0.2
9.18	32.5	10.94	2.09	0.2
15.66	70.8	16.23	2.01	0.18
12.05	69.3	13.92	2.01	0.18
8.43	51.7	11.64	2.68	0.02
13.38	33.1	14.07	2.31	0.07
10.48	41.9	12.23	2.37	0.43
11.97	27.2	12.75	2.32	0.2
12.21	72.3	14.06	2.51	0.14
13.29	8.4	13.36	1.95	0.12
14.40	68.2	15.41	2.53	0.27
10.42	66.6	12.85	2.53	0.27
13.31	84.4	14.82	2.1	0.21
14.76	70.6	15.65	2.1	0.21
9.38	89.1	12.71	1.92	0.08
12.98	30.3	13.67	1.92	0.08
13.57	71.7	14.91	1.92	0.08
11.36	47.5	13.02	2.34	0.15
11.56	74.0	13.67	2.34	0.15
11.54	55.8	13.36	2.34	0.15
14.26	78.2	15.38	2.34	0.15
11.54	86.9	13.74	2.52	0.12
16.44	49.6	16.65	2.52	0.12
12.97	59.6	14.37	3.2	0.26
9.29	56.9	11.99	3.2	0.26
14.34	38.6	14.95	2.48	0.25
10.84	44.1	12.55	2.4	0.1
9.36	80.0	12.61	2.4	0.1
12.12	61.2	13.84	2.52	0.2
15.65	46.1	16.05	2.52	0.2
11.39	49.6	13.1	3.08	0.41
12.46	50.9	13.86	3.08	0.41
8.44	57.9	11.87	3.08	0.41
13.95	48.1	14.84	2.11	0.3
9.15	72.5	12.41	2.11	0.3
11.90	46.6	13.36	2.54	0.41

14.99	29.0	15.31	2.54	0.41
13.96	71.6	15.15	2.03	0.22
11.51	51.5	13.23	2.27	0.17
10.72	76.3	13.17	1.97	0.28
13.00	53.4	14.28	2.17	0.27
13.48	41.8	14.37	2.17	0.27
3.57	40.9	10.36	2.17	0.27
13.72	67.8	14.96	2.76	0.15
7.42	55.5	11.61	2.76	0.15
14.84	38.9	15.34	2.34	0.24
11.74	37.5	12.96	2.34	0.24
13.56	33.0	14.21	2.34	0.24
14.10	56.9	15.08	2.45	0.29
7.48	70.3	12.02	2.45	0.29
10.73	55.1	12.81	2.45	0.29
10.72	35.0	12.13	2.45	0.29
8.78	84.4	12.53	2.45	0.29
13.29	69.1	14.7	2.67	0.34
10.26	49.9	12.36	2.67	0.34
13.09	61.9	14.49	2.23	0.22
14.43	72.6	15.46	2.71	0.18
14.06	82.7	15.27	2.71	0.18
12.66	88.4	14.42	2.36	0.3
9.76	78.7	12.69	2.36	0.3
11.89	67.7	13.8	2.65	0.24

Table S4.3 – Apatite fission-track analytical results. Ns = number of spontaneous fission tracks; ρs = fission track density; zeta = 3.574 ± 0.1325; G = 1; λ-α = 1.551E-10, decay constants from Jaffey, A.H., Flynn, K.F., Glendenin, L.E., Bentley, W.C., Essling, A.M., 1971. Precision measurement of the half-lives and specific activities of 235U and 238U. Phys. Rev. 4, 1889– 1906. Age calculation after Donelick, R.A., O'Sullivan, P.B., Ketcham, R.A., 2005. Apatite fission-track analysis. Rev. Mineral. Geochem. 58, 49–94.

Sample BR-3

Sample ID	Ns	ρs	counted units	unit size (cm^2)	area (cm^2)	^{238}U/^{43}Ca	1σ [^{238}U/^{43}Ca]	**Age [Ma]**	**Error [Ma]**
154-14-1	47	1.57E+06	30	1.00E-06	3.00E-05	0.0428	0.0013	**129.5**	**19.9**
154-14-2	67	1.60E+06	42	1.00E-06	4.20E-05	0.046	0.0019	**122.8**	**16.5**
154-14-3	20	8.00E+05	25	1.00E-06	2.50E-05	0.0304	0.0044	**93.4**	**25.1**
154-14-4	27	5.00E+05	54	1.00E-06	5.40E-05	0.01656	0.00066	**107.0**	**21.4**
154-14-5	21	5.25E+05	40	1.00E-06	4.00E-05	0.01545	0.00067	**120.3**	**27.1**
154-14-6	29	9.67E+05	30	1.00E-06	3.00E-05	0.02112	0.0008	**161.5**	**31.2**
154-14-7	39	1.56E+06	25	1.00E-06	2.50E-05	0.0623	0.0022	**88.9**	**14.9**
154-14-8	35	8.33E+05	42	1.00E-06	4.20E-05	0.02845	0.00093	**103.8**	**18.3**
154-14-9	28	1.12E+06	25	1.00E-06	2.50E-05	0.0303	0.0026	**130.8**	**27.6**
154-14-10	31	8.86E+05	35	1.00E-06	3.50E-05	0.03492	0.00075	**90.0**	**16.6**
154-14-11	15	4.17E+05	36	1.00E-06	3.60E-05	0.01142	0.00045	**129.1**	**34.1**
154-14-12	36	1.00E+06	36	1.00E-06	3.60E-05	0.02401	0.00078	**147.2**	**25.6**
154-14-13	35	1.40E+06	25	1.00E-06	2.50E-05	0.086	0.075	**57.9**	**51.5**
154-14-14	38	9.05E+05	42	1.00E-06	4.20E-05	0.02964	0.00091	**108.2**	**18.3**
154-14-15	36	1.13E+06	32	1.00E-06	3.20E-05	0.0543	0.001	**73.6**	**12.6**
154-14-16	24	6.86E+05	35	1.00E-06	3.50E-05	0.03252	0.00081	**74.9**	**15.7**
154-14-17	40	1.33E+06	30	1.00E-06	3.00E-05	0.03515	0.00069	**134.2**	**21.9**
154-14-19	16	6.40E+05	25	1.00E-06	2.50E-05	0.04207	0.00075	**54.1**	**13.7**
154-14-21	99	3.54E+06	28	1.00E-06	2.80E-05	0.1118	0.0041	**112.0**	**12.7**
154-14-22	90	2.25E+06	40	1.00E-06	4.00E-05	0.0989	0.0016	**80.8**	**9.1**
154-14-23	48	1.33E+06	36	1.00E-06	3.60E-05	0.03694	0.00067	**127.7**	**19.2**
154-14-26	8	2.86E+05	28	1.00E-06	2.80E-05	0.01241	0.00047	**81.8**	**29.2**
154-14-27	8	1.63E+05	49	1.00E-06	4.90E-05	0.00775	0.00048	**74.8**	**27.0**
154-14-28	27	9.00E+05	30	1.00E-06	3.00E-05	0.02891	0.00081	**110.3**	**21.8**
154-14-30	6	1.71E+05	35	1.00E-06	3.50E-05	0.00317	0.00029	**190.4**	**80.0**
154-14-31	4	1.14E+05	35	1.00E-06	3.50E-05	0.0406	0.0023	**10.1**	**5.1**
154-14-32	16	8.00E+05	20	1.00E-06	2.00E-05	0.01188	0.00097	**236.3**	**62.8**
154-14-33	13	6.50E+05	20	1.00E-06	2.00E-05	0.02721	0.00069	**84.8**	**23.8**

Sample BR-4

Sample ID	Ns	ρs	counted units	unit size (cm^2)	area (cm^2)	$^{238}U/^{43}Ca$	1σ [$^{238}U/^{43}Ca$]	**Age [Ma]**	**Error [Ma]**
154-15-1	32	1.33E+06	24	1.00E-06	2.40E-05	0.0592	0.0028	**80.0**	**14.9**
154-15-2	13	3.61E+05	36	1.00E-06	3.60E-05	0.02406	0.00081	**53.4**	**15.1**
154-15-3	15	3.75E+05	40	1.00E-06	4.00E-05	0.00831	0.00036	**159.3**	**42.1**
154-15-4	65	1.55E+06	42	1.00E-06	4.20E-05	0.035	0.003	**156.1**	**24.2**
154-15-5	79	3.16E+06	25	1.00E-06	2.50E-05	0.1417	0.004	**79.2**	**9.6**
154-15-6	24	6.67E+05	36	1.00E-06	3.60E-05	0.02169	0.00081	**108.9**	**23.0**
154-15-8	37	1.54E+06	24	1.00E-06	2.40E-05	0.02699	0.00088	**201.0**	**34.5**
154-15-9	14	2.80E+05	50	1.00E-06	5.00E-05	0.01651	0.00066	**60.3**	**16.5**
154-15-10	29	9.67E+05	30	1.00E-06	3.00E-05	0.0346	0.00072	**99.1**	**18.9**
154-15-11	32	8.89E+05	36	1.00E-06	3.60E-05	0.0444	0.0011	**71.2**	**13.0**
154-15-12	47	1.57E+06	30	1.00E-06	3.00E-05	0.08035	0.00088	**69.3**	**10.5**
154-15-13	11	4.58E+05	24	1.00E-06	2.40E-05	0.01471	0.00062	**110.4**	**33.9**
154-15-14	15	6.00E+05	25	1.00E-06	2.50E-05	0.02256	0.00058	**94.4**	**24.7**
154-15-15	20	6.67E+05	30	1.00E-06	3.00E-05	0.0426	0.0059	**55.7**	**14.8**
154-15-16	49	1.96E+06	25	1.00E-06	2.50E-05	0.0521	0.0018	**133.1**	**20.2**
154-15-18	56	1.56E+06	36	1.00E-06	3.60E-05	0.0621	0.0037	**88.9**	**13.4**
154-15-19	65	1.30E+06	50	1.00E-06	5.00E-05	0.0827	0.0024	**55.9**	**7.4**
154-15-20	63	2.52E+06	25	1.00E-06	2.50E-05	0.1551	0.0069	**57.8**	**8.0**
154-15-21	16	6.40E+05	25	1.00E-06	2.50E-05	0.01688	0.00065	**134.1**	**34.3**
154-15-22	15	3.75E+05	40	1.00E-06	4.00E-05	0.0174	0.002	**76.6**	**21.8**
154-15-23	78	3.25E+06	24	1.00E-06	2.40E-05	0.2183	0.0058	**53.0**	**6.5**
154-15-24	13	4.33E+05	30	1.00E-06	3.00E-05	0.03141	0.00082	**49.1**	**13.8**
154-15-25	14	7.00E+05	20	1.00E-06	2.00E-05	0.0239	0.0015	**103.8**	**28.8**
154-15-26	2	4.08E+04	49	1.00E-06	4.90E-05	0.00095	0.00011	**151.7**	**108.9**
154-15-27	33	7.33E+05	45	1.00E-06	4.50E-05	0.0257	0.0015	**101.2**	**19.0**
154-15-28	17	5.67E+05	30	1.00E-06	3.00E-05	0.01164	0.00054	**171.7**	**42.9**
154-15-29	15	3.57E+05	42	1.00E-06	4.20E-05	0.0153	0.00057	**82.9**	**21.8**
154-15-30	24	1.14E+06	21	1.00E-06	2.10E-05	0.0639	0.0038	**63.6**	**13.7**
154-15-31	35	1.46E+06	24	1.00E-06	2.40E-05	0.0642	0.0043	**80.7**	**15.0**
154-15-32	11	3.44E+05	32	1.00E-06	3.20E-05	0.089	0.015	**13.8**	**4.8**

Sample BR-6

Sample ID	Ns	ρs	counted units	unit size (cm^2)	area (cm^2)	^{238}U/^{43}Ca	1σ [^{238}U/^{43}Ca]	**Age [Ma]**	**Error [Ma]**
154-05-2	47	1.12E+06	42	1.00E-06	4.20E-05	0.0365	0.0013	**108.6**	**16.8**
154-05-3	48	1.20E+06	40	1.00E-06	4.00E-05	0.04905	0.00068	**86.8**	**13.0**
154-05-5	13	3.25E+05	40	1.00E-06	4.00E-05	0.01176	0.00032	**98.0**	**27.6**
154-05-6	12	3.00E+05	40	1.00E-06	4.00E-05	0.00977	0.00047	**108.8**	**32.1**
154-05-7	15	6.25E+05	24	1.00E-06	2.40E-05	0.00762	0.00081	**286.7**	**80.7**
154-05-8	18	7.50E+05	24	1.00E-06	2.40E-05	0.0513	0.0011	**52.0**	**12.5**
154-05-9	29	1.04E+06	28	1.00E-06	2.80E-05	0.044	0.0029	**83.6**	**16.8**
154-05-10	26	1.08E+06	24	1.00E-06	2.40E-05	0.01719	0.00062	**221.4**	**44.9**
154-05-12	24	1.00E+06	24	1.00E-06	2.40E-05	0.0409	0.0014	**86.8**	**18.2**
154-05-16	20	8.00E+05	25	1.00E-06	2.50E-05	0.037	0.0011	**76.8**	**17.6**
154-05-17	9	5.63E+05	16	1.00E-06	1.60E-05	0.01006	0.00039	**196.8**	**66.4**
154-05-18	23	5.48E+05	42	1.00E-06	4.20E-05	0.01442	0.00061	**134.3**	**29.0**
154-05-19	57	2.38E+06	24	1.00E-06	2.40E-05	0.0918	0.0027	**91.8**	**12.9**
154-05-20	13	4.64E+05	28	1.00E-06	2.80E-05	0.01397	0.00049	**117.7**	**33.2**
154-05-21	10	3.33E+05	30	1.00E-06	3.00E-05	0.00621	0.00024	**189.0**	**60.6**
154-05-22	13	4.33E+05	30	1.00E-06	3.00E-05	0.0176	0.00049	**87.4**	**24.6**
154-05-23	41	9.11E+05	45	1.00E-06	4.50E-05	0.023	0.0011	**140.0**	**23.5**
154-05-24	54	1.29E+06	42	1.00E-06	4.20E-05	0.0547	0.0033	**83.5**	**12.8**
154-05-25	14	5.60E+05	25	1.00E-06	2.50E-05	0.0319	0.0012	**62.4**	**17.0**
154-05-26	16	6.40E+05	25	1.00E-06	2.50E-05	0.01689	0.00056	**134.0**	**34.2**
154-05-27	6	2.50E+05	24	1.00E-06	2.40E-05	0.00651	0.00032	**135.8**	**56.1**
154-05-29	7	2.33E+05	30	1.00E-06	3.00E-05	0.0064	0.00038	**129.0**	**49.6**
154-05-30	32	1.14E+06	28	1.00E-06	2.80E-05	0.03749	0.00099	**108.0**	**19.7**
154-05-31	18	4.00E+05	45	1.00E-06	4.50E-05	0.00475	0.00033	**294.1**	**73.1**
154-05-32	20	6.25E+05	32	1.00E-06	3.20E-05	0.02228	0.00063	**99.5**	**22.7**
154-05-33	36	1.20E+06	30	1.00E-06	3.00E-05	0.0353	0.0012	**120.4**	**21.0**

Sample BR-7

Sample ID	Ns	ρs	counted units	unit size (cm^2)	area (cm^2)	^{238}U/^{43}Ca	1σ [^{238}U/^{43}Ca]	**Age [Ma]**	**Error [Ma]**
154-08-1	6	1.20E+05	50	1.00E-06	5.00E-05	0.00508	0.00022	**83.9**	**34.6**
154-08-2	98	1.75E+06	56	1.00E-06	5.60E-05	0.0876	0.0022	**71.0**	**7.8**
154-08-3	33	1.18E+06	28	1.00E-06	2.80E-05	0.02774	0.00087	**150.1**	**27.1**
154-08-4	12	7.50E+05	16	1.00E-06	1.60E-05	0.01936	0.0005	**137.0**	**40.0**
154-08-5	18	5.00E+05	36	1.00E-06	3.60E-05	0.00986	0.00032	**178.7**	**43.0**
154-08-6	36	7.20E+05	50	1.00E-06	5.00E-05	0.01012	0.00041	**249.4**	**43.8**
154-08-8	24	8.00E+05	30	1.00E-06	3.00E-05	0.0222	0.0008	**127.5**	**26.9**
154-08-9	10	2.86E+05	35	1.00E-06	3.50E-05	0.00552	0.00031	**182.4**	**59.0**
154-08-10	16	5.33E+05	30	1.00E-06	3.00E-05	0.01911	0.0006	**99.0**	**25.2**
154-08-11	6	2.86E+05	21	1.00E-06	2.10E-05	0.0097	0.00025	**104.4**	**42.9**
154-08-12	14	5.60E+05	25	1.00E-06	2.50E-05	0.0464	0.0025	**43.0**	**11.8**
154-08-14	19	4.75E+05	40	1.00E-06	4.00E-05	0.01139	0.00042	**147.3**	**34.7**
154-08-15	19	6.33E+05	30	1.00E-06	3.00E-05	0.04324	0.0009	**52.1**	**12.2**
154-08-16	46	2.30E+06	20	1.00E-06	2.00E-05	0.1285	0.0048	**63.7**	**10.0**
154-08-17	13	6.19E+05	21	1.00E-06	2.10E-05	0.02558	0.00064	**85.9**	**24.1**
154-08-18	12	2.40E+05	50	1.00E-06	5.00E-05	0.00865	0.00034	**98.4**	**28.9**
154-08-19	7	2.92E+05	24	1.00E-06	2.40E-05	0.01093	0.00038	**94.7**	**36.1**
154-08-20	15	3.06E+05	49	1.00E-06	4.90E-05	0.01168	0.00042	**93.0**	**24.5**
154-08-21	30	1.25E+06	24	1.00E-06	2.40E-05	0.04376	0.00087	**101.3**	**19.0**
154-08-22	13	4.06E+05	32	1.00E-06	3.20E-05	0.0095	0.0013	**151.0**	**47.0**
154-08-13	31	1.11E+06	28	1.00E-06	2.80E-05	0.01654	0.00061	**234.9**	**43.9**
154-08-23	18	4.50E+05	40	1.00E-06	4.00E-05	0.0171	0.0015	**93.4**	**23.7**
154-08-24	21	5.00E+05	42	1.00E-06	4.20E-05	0.02219	0.00054	**80.0**	**17.8**
154-08-25	8	4.00E+05	20	1.00E-06	2.00E-05	0.01841	0.00055	**77.2**	**27.5**
154-08-26	18	7.20E+05	25	1.00E-06	2.50E-05	0.01549	0.00045	**164.0**	**39.4**
154-08-27	11	4.40E+05	25	1.00E-06	2.50E-05	0.0267	0.001	**58.6**	**17.9**
154-08-28	10	4.17E+05	24	1.00E-06	2.40E-05	0.0136	0.0014	**108.6**	**36.3**
154-08-29	54	2.25E+06	24	1.00E-06	2.40E-05	0.0896	0.0034	**89.1**	**13.0**
154-08-30	12	7.50E+05	16	1.00E-06	1.60E-05	0.039	0.003	**68.4**	**20.6**
154-08-31	16	6.40E+05	25	1.00E-06	2.50E-05	0.0376	0.00085	**60.5**	**15.4**
154-08-32	15	7.50E+05	20	1.00E-06	2.00E-05	0.00964	0.00076	**272.2**	**74.2**
154-08-33	47	1.88E+06	25	1.00E-06	2.50E-05	0.04597	0.00098	**144.5**	**22.0**

Sample BR-9

Sample ID	Ns	ρs	counted units	unit size (cm^2)	area (cm^2)	$^{238}U/^{43}Ca$	1σ [$^{238}U/^{43}Ca$]	**Age [Ma]**	**Error [Ma]**
154-01-1	39	8.67E+05	45	1.00E-06	4.50E-05	0.01468	0.00046	**207.6**	**34.7**
154-01-2	33	6.11E+05	54	1.00E-06	5.40E-05	0.02564	0.00062	**84.6**	**15.2**
154-01-3	56	1.40E+06	40	1.00E-06	4.00E-05	0.0359	0.0025	**137.9**	**21.4**
154-01-4	52	1.73E+06	30	1.00E-06	3.00E-05	0.0611	0.0013	**100.6**	**14.6**
154-01-5	83	2.08E+06	40	1.00E-06	4.00E-05	0.1384	0.0027	**53.4**	**6.3**
154-01-6	44	1.57E+06	28	1.00E-06	2.80E-05	0.0511	0.0016	**109.0**	**17.3**
154-01-7	118	2.19E+06	54	1.00E-06	5.40E-05	0.0788	0.0076	**98.3**	**13.6**
154-01-8	26	1.08E+06	24	1.00E-06	2.40E-05	0.03401	0.00068	**112.8**	**22.6**
154-01-9	26	1.44E+06	18	1.00E-06	1.80E-05	0.055	0.0011	**93.2**	**18.7**
154-01-10	18	5.14E+05	35	1.00E-06	3.50E-05	0.01642	0.0006	**111.0**	**26.8**
154-01-11	36	8.57E+05	42	1.00E-06	4.20E-05	0.0572	0.0025	**53.3**	**9.4**
154-01-12	36	1.03E+06	35	1.00E-06	3.50E-05	0.0491	0.0013	**74.4**	**12.9**
154-01-13	27	6.75E+05	40	1.00E-06	4.00E-05	0.0243	0.0015	**98.5**	**20.2**
154-01-15	24	9.60E+05	25	1.00E-06	2.50E-05	0.03226	0.00061	**105.5**	**22.0**
154-01-16	49	2.45E+06	20	1.00E-06	2.00E-05	0.1137	0.0018	**76.6**	**11.4**
154-01-17	36	6.00E+05	60	1.00E-06	6.00E-05	0.04269	0.00087	**50.0**	**8.6**
154-01-18	43	2.05E+06	21	1.00E-06	2.10E-05	0.04715	0.00069	**153.4**	**24.2**
154-01-20	47	1.57E+06	30	1.00E-06	3.00E-05	0.0999	0.0018	**55.8**	**8.5**
154-01-21	99	2.36E+06	42	1.00E-06	4.20E-05	0.0954	0.0017	**87.7**	**9.5**
154-01-22	27	7.71E+05	35	1.00E-06	3.50E-05	0.02288	0.00053	**119.4**	**23.6**
154-01-23	50	1.19E+06	42	1.00E-06	4.20E-05	0.0373	0.0026	**113.1**	**18.3**
154-01-24	34	7.08E+05	48	1.00E-06	4.80E-05	0.02551	0.00073	**98.5**	**17.5**
154-01-25	17	4.05E+05	42	1.00E-06	4.20E-05	0.02486	0.00038	**57.9**	**14.2**
154-01-26	46	7.67E+05	60	1.00E-06	6.00E-05	0.0348	0.0016	**78.3**	**12.4**
154-01-27	39	1.08E+06	36	1.00E-06	3.60E-05	0.03146	0.00095	**121.9**	**20.4**
154-01-28	24	8.00E+05	30	1.00E-06	3.00E-05	0.038	0.0012	**74.8**	**15.7**
154-01-30	37	1.03E+06	36	1.00E-06	3.60E-05	0.05742	0.00087	**63.7**	**10.8**
154-01-31	79	3.95E+06	20	1.00E-06	2.00E-05	0.1556	0.0045	**90.1**	**11.0**
154-01-32	84	2.63E+06	32	1.00E-06	3.20E-05	0.0963	0.0055	**96.7**	**12.4**

Sample BR-10

Sample ID	Ns	ρs	counted units	unit size (cm^2)	area (cm^2)	$^{238}U/^{43}Ca$	1σ $[^{238}U/^{43}Ca]$	**Age [Ma]**	**Error [Ma]**
154-02-2	10	3.57E+05	28	1.00E-06	2.80E-05	0.01557	0.0004	**81.5**	**26.0**
154-02-4	9	2.81E+05	32	1.00E-06	3.20E-05	0.00942	0.00056	**105.8**	**36.0**
154-02-10	31	8.86E+05	35	1.00E-06	3.50E-05	0.03025	0.00081	**103.8**	**19.2**
154-02-13	48	1.14E+06	42	1.00E-06	4.20E-05	0.0575	0.0015	**70.6**	**10.7**
154-02-14	37	1.16E+06	32	1.00E-06	3.20E-05	0.04513	0.00088	**90.9**	**15.4**
154-02-15	12	2.50E+05	48	1.00E-06	4.80E-05	0.00399	0.00023	**220.1**	**65.3**
154-02-16	28	1.00E+06	28	1.00E-06	2.80E-05	0.0216	0.0031	**163.4**	**39.2**
154-02-17	67	2.68E+06	25	1.00E-06	2.50E-05	0.1347	0.0029	**70.7**	**9.2**
154-02-21	13	2.71E+05	48	1.00E-06	4.80E-05	0.00624	0.0003	**153.3**	**43.5**
154-02-23	15	6.25E+05	24	1.00E-06	2.40E-05	0.01567	0.0005	**141.0**	**37.1**
154-02-25	12	4.00E+05	30	1.00E-06	3.00E-05	0.0073	0.00027	**192.9**	**56.6**
154-02-26	23	9.20E+05	25	1.00E-06	2.50E-05	0.0225	0.0006	**144.5**	**30.8**
154-02-29	9	2.57E+05	35	1.00E-06	3.50E-05	0.01053	0.00037	**86.7**	**29.2**
154-02-30	7	2.19E+05	32	1.00E-06	3.20E-05	0.00387	0.00026	**198.9**	**76.7**
154-02-31	36	1.03E+06	35	1.00E-06	3.50E-05	0.02168	0.00092	**167.4**	**29.4**
154-02-32	21	7.50E+05	28	1.00E-06	2.80E-05	0.0215	0.0011	**123.5**	**28.1**
154-02-33	18	5.00E+05	36	1.00E-06	3.60E-05	0.00917	0.00057	**192.0**	**47.3**

Supplementary Information 5 – Apatite (U-Th)/He and fission track single grain ages with respect to relevant geologic events

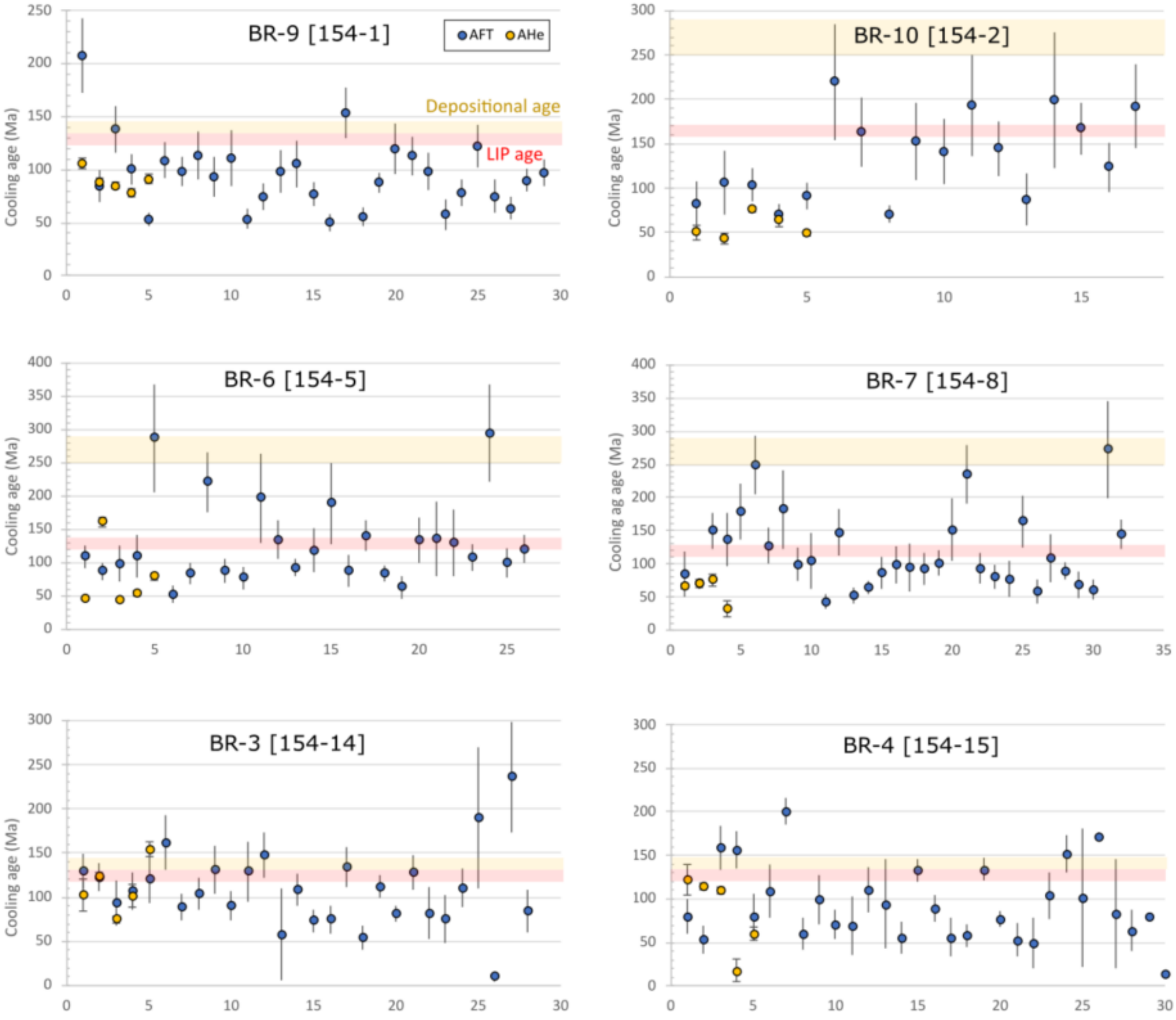

Fig. S5.1 – Apatite (U-Th)/He and fission track single grain ages with respect to relevant geologic events. The x-axis represents the grain # in each sample.

Supplementary Information 6 – Inverse thermal history model results

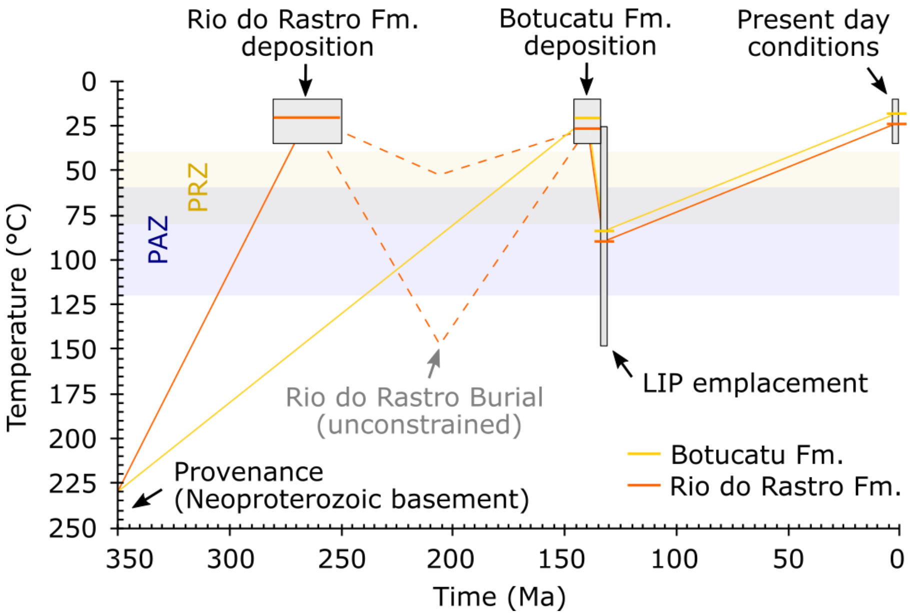

Fig. S6.1 – Graphical representation of modelling constraints

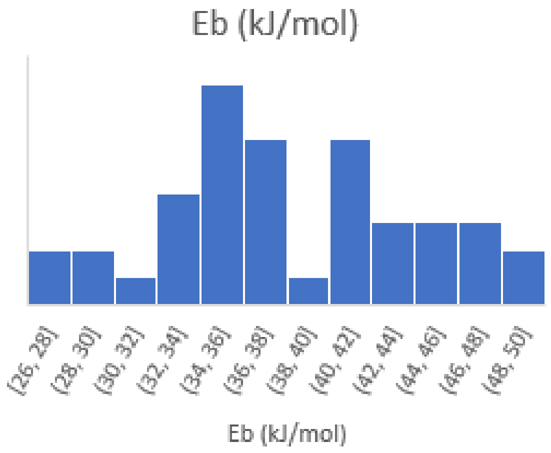

Fig. S6.2 – Histogram of resampled Eb values

Supplementary Information 7 – AFT and AHe data compilation

Table S7.1 – AFT data compilation

Sample information					Distance to coast	Distance to scarp	Norm. distance to	Age (Ma)					Track Length (µm)					Dpar (µm)					Geological information			Reference
Sample	Lat	Long	Elevation (m)	Depth (m)	(Km)	(Km)	coast	N	Central Age		1σ	P (χ2) (%)	n	Mean		1σ	Std	n	Mean		1σ	Skew	Unit	Lithology	Formation Age	
10a	-28.394	-49.527	740	-	50.073	2.07	1.04	12	88.6	±	5.0	70	26	13.15	±	0.25	1.25	-	-	±	-	-	Botucatu Fm.	Sandstone	Early Cretaceous	Gallagher et al. (1994)
10b	-28.394	-49.527	740	-	50.073	2.07	1.04	19	95.4	±	4.0	80	89	12.72	±	0.23	1.62	-	-	±	-	-	Botucatu Fm.	Sandstone	Early Cretaceous	Gallagher et al. (1994)
10c	-28.394	-49.527	740	-	50.073	2.07	1.04	12	92.3	±	7.0	40	27	12.58	±	0.35	1.78	-	-	±	-	-	Botucatu Fm.	Sandstone	Early Cretaceous	Gallagher et al. (1994)
10d	-28.394	-49.527	740	-	50.073	2.07	1.04	20	81	±	6.0	8	45	12.71	±	0.27	1.81	-	-	±	-	-	Botucatu Fm.	Sandstone	Early Cretaceous	Gallagher et al. (1994)
10e	-28.394	-49.527	740	-	50.073	2.07	1.04	14	74.8	±	4.0	85	5	12.93	±	0.66	1.32	-	-	±	-	-	Botucatu Fm.	Sandstone	Early Cretaceous	Gallagher et al. (1994)
10f	-28.394	-49.527	740	-	50.073	2.07	1.04	18	88	±	7.0	1	17	12.66	±	0.72	2.88	-	-	±	-	-	Botucatu Fm.	Sandstone	Early Cretaceous	Gallagher et al. (1994)
2a	-29.358	-49.734	2	-	0	-28.915	0.00	15	123.7	±	7.0	70	41	13.38	±	0.2	1.28	-	-	±	-	-	Botucatu Fm.	Sandstone	Early Cretaceous	Gallagher et al. (1994)
2b	-29.358	-49.734	1	-	0	-28.915	0.00	1	121.2	±	27.0	-	0		±	-	-	-	-	±	-	-	Botucatu Fm.	Sandstone	Early Cretaceous	Gallagher et al. (1994)
2c	-29.358	-49.734	0	-	0	-28.915	0.00	7	101	±	10.0	25	5	13.65	±	0.32	0.64	-	-	±	-	-	Botucatu Fm.	Sandstone	Early Cretaceous	Gallagher et al. (1994)
3	-28.383	-49.032	109	-	11.925	-46.398	0.20	19	52.2	±	5.0	2	24	13.29	±	0.35	1.7	-	-	±	-	-	Basement	Granite	Neoproterozoic	Gallagher et al. (1994)
4	-28.338	-49.202	120	-	27.998	-33.134	0.46	14	64.7	±	6.0	20	64	13.07	±	0.26	2.06	-	-	±	-	-	Basement	Granite	Neoproterozoic	Gallagher et al. (1994)
5	-28.360	-49.330	130	-	36.884	-18.687	0.66	24	67.5	±	3.0	0	40	12.74	±	0.23	1.45	-	-	±	-	-	Basement	Granite	Neoproterozoic	Gallagher et al. (1994)
6	-28.390	-49.380	150	-	38.889	-13.44	0.74	20	82.3	±	4.0	0	98	12.83	±	0.21	2.09	-	-	±	-	-	Basement	Granite	Neoproterozoic	Gallagher et al. (1994)
7	-28.386	-49.490	550	-	47.919	-0.96	0.98	18	150.3	±	16.0	0	71	12.41	±	0.29	2.42	-	-	±	-	-	NA - Serra Alta/Teresina Fm.?	Sedimentary	-	Gallagher et al. (1994)
8	-28.386	-49.494	555	-	47.919	-0.96	0.98	21	157	±	14.0	0	100	12.85	±	0.19	1.93	-	-	±	-	-	NA - Serra Alta/Teresina Fm.?	Sedimentary	-	Gallagher et al. (1994)
9	-28.389	-49.505	600	-	48.74	0.1	1.00	6	141.2	±	13.0	20	11	12.68	±	0.6	1.89	-	-	±	-	-	NA - Serra Alta/Teresina Fm.?	Sedimentary	-	Gallagher et al. (1994)
11	-28.112	-49.499	1650	-	68.805	8.295	1.14	20	123.7	±	6.0	5	59	14.14	±	0.19	1.47	-	-	±	-	-	Serra Geral Gr.	Basalt	Early Cretaceous	Gallagher et al. (1994)
12	-28.121	-49.478	1750	-	68.805	8.295	1.14	27	132.3	±	5.0	10	43	15.1	±	0.27	1.72	-	-	±	-	-	Serra Geral Gr.	Basalt	Early Cretaceous	Gallagher et al. (1994)
13	-28.100	-49.450	1160	-	63.538	7.721	1.14	10	95.7	±	6.0	100	51	12.75	±	0.35	2.46	-	-	±	-	-	Botucatu Fm.	Sedimentary	Early Cretaceous	Gallagher et al. (1994)
14	-28.090	-49.440	1100	-	63.519	9.1	1.17	11	99.4	±	8.0	5	12	13.25	±	0.41	1.35	-	-	±	-	-	Botucatu Fm.	Sedimentary	Early Cretaceous	Gallagher et al. (1994)
15	-28.080	-49.400	1005	-	60.959	3.7	1.06	9	90.1	±	10.0	5	15	12.86	±	0.27	1	-	-	±	-	-	Botucatu Fm.	Sedimentary	Early Cretaceous	Gallagher et al. (1994)
16	-28.140	-49.270	170	-	46.641	-11.805	0.80	16	60.7	±	4.0	0	27	12.13	±	0.43	2.21	-	-	±	-	-	Basement	Granite	Neoproterozoic	Gallagher et al. (1994)
17	-28.190	-49.230	90	-	40.296	-19.424	0.67	18	77	±	8.0	0	53	12.25	±	0.32	2.34	-	-	±	-	-	Basement	Granite	Neoproterozoic	Gallagher et al. (1994)
BR09-50	*-28.697*	*-49.178*	27	-	2.65	-41.9	0.06	21	76.2	±	6.6	99.2	80	13.0	±	-	1.7	160	1.3	±	0.1	1.5	Basement	Granite	Neoproterozoic	Karl et al. (2013)
BR09-51	*-28.580*	*-49.052*	7	-	0.42	-50.3	0.01	25	76.7	±	6.1	100.0	10	13.7	±	-	1.2	175	1.4	±	0.1	1.7	Basement	Granite	Neoproterozoic	Karl et al. (2013)
BR09-52	*-28.447*	*-48.968*	13	-	2.68	-56.36	0.05	21	73.4	±	5.6	99.6	78	12.9	±	-	2.1	145	1.3	±	0.1	1.6	Basement	Granite	Neoproterozoic	Karl et al. (2013)
BR09-53	-28.426	-48.858	20	-	64	0	0.00	24	70.7	±	4.6	98.9	10	13.1	±	-	1.8	165	1.3	±	0.1	1.5	Basement	Granite	Neoproterozoic	Karl et al. (2013)
BR09-45	-28.361	-49.306	194	-	35.016	-20.72	0.63	20	76.4	±	5.9	58.7	95	12.9	±	-	1.2	140	1.4	±	0.1	1.5	Basement	Granodiorite	Neoproterozoic	Karl et al. (2013)
BR09-46	-28.295	-49.114	133	-	24.236	-33.25	0.42	23	69.8	±	5.6	99.9	93	12.1	±	-	1.7	165	1.4	±	0.2	1.6	Basement	Granite	Neoproterozoic	Karl et al. (2013)
BR09-42	-28.394	-49.527	740	-	50.073	2.07	1.04	19	59.5	±	5.2	1.0	-	-	±	-	-	-	-	±	-	-	Botucatu Fm.	Sandstone	Early Cretaceous	Karl et al. (2013)
BR09-35	-27.867	-50.193	931	-	137.206	85.78	2.67	5	79.7	±	10.9	89.8	-	-	±	-	-	5	1.2	±	0.1	0.2	Botucatu Fm.	Sandstone	Jurassic	Karl et al. (2013)
BR09-17	*-26.201*	*-51.521*	*903*	-	*353.747*	*290.338*	*5.58*	*5*	*47.7*	*±*	*11.0*	*91.4*	-	-	±	-	-	*12*	*1.0*	*±*	*0.3*	*0.5*	Serra Geral Gr.	Basalt	Early Cretaceous	Karl et al. (2013)
BR10-32	-27.931	-48.661	17	-	12.242	-56.515	0.18	23	78.0	±	5.8	98.5	55	14.0	±	-	1.3	243	1.3	±	0.2	0.2	Basement	Granite	Neoproterozoic	Krob et al. (2019)
BR10-34	-28.252	-48.702	20	-	0	-68.98	0.00	18	68.4	±	5.2	76.7	10	13.4	±	-	1.3	90	1.5	±	0.2	-0.2	Basement	Granite	Neoproterozoic	Krob et al. (2019)
PDM 9	-28.535	-49.421	-	305	32.3	-11.913	0.73	2	221.6	±	14.9	8.8	-	-	±	-	-	-	-	±	-	-	Rio Bonito Fm.	Sandstone	Carboniferous–Permian	Bicca et al. (2020)
PDM 10	-28.535	-49.421	-	309	32.3	-11.913	0.73	5	77.0	±	8.8	-	-	-	±	-	-	-	-	±	-	-	Rio Bonito Fm.	Sandstone	Carboniferous–Permian	Bicca et al. (2020)
PDM 11	-28.480	-49.463	-	95	39.282	-5.963	0.87	6	57.3	±	7.6	0.7	3	11.40	±	0.7	0.8	-	7	±	-	-	Rio Bonito Fm.	Sandstone	Carboniferous–Permian	Bicca et al. (2020)
PDM 12	-28.750	-49.237	-	41	3.737	-37.478	0.09	3	46.2	±	6.8	0.0	3	10.26	±	0.8	0.3	-	4	±	-	-	Rio Bonito Fm.	Sandstone	Carboniferous–Permian	Bicca et al. (2020)
PDM 13	-28.750	-49.237	-	62	3.737	-37.478	0.09	24	52.7	±	7.3	0.0	8	-	±		-	-	-	±	-	-	Rio Bonito Fm.	Sandstone	Carboniferous–Permian	Bicca et al. (2020)
PDM 14	-28.730	-49.361	-	68	14.75	-25.669	0.36	33	168.6	±	13.0	0.0	16	-	±		-	-	-	±	-	-	Rio Bonito Fm.	Sandstone	Carboniferous–Permian	Bicca et al. (2020)

Table S7.2 – AHe data compilation

Sample	n	Region	Reference	Lat	Lon	Z	Lithology and/or formation	Stratigraphy age (Ma or age)	Distance to coast (km)	n	Average corr. AHe (Ma)	AHe error	Error %	Min AHe (Ma)		Max AHe (Ma)	Age crystal 1	Age crystal 2	Age crystal 3	Age crystal 4	Age crystal 5	Age crystal 6	Age crystal 7
BR-9	1	Study area	*This study*	-28.394	-49.527	740	Sandstone - Botucatu Fm	Early Cretaceous	50.1	5	89.66	4.63	5%	77.9	-	105.9	105.92	88.31	84.87	77.93	91.25		
BR-10	2	Study area	*This study*	-28.388	-49.510	637	Sandstone - Rio do Rasto Fm.	Upper Permian	49.1	5	56.29	6.05	11%	42.8	-	76.4	49.98	42.82	76.36	63.52	48.78		
BR-6	3	Study area	*This study*	-28.891	-49.831	131	Sandstone - Rio do Rasto Fm.	Upper Permian	40.9	4	55.75	8.02	14%	44.3	-	78.9	45.83	44.28	53.96	78.94			
BR-7	4	Study area	*This study*	-28.938	-49.622	12	Sandstone - Rio do Rasto Fm.	Upper Permian	21.4	3	70.51	2.73	4%	66.1	-	75.5	66.08	69.96	75.49				
BR-8	5	Study area	*This study*	-28.942	-49.367	30	Sandstone - Rio do Rasto Fm.	Upper Permian	1.1	7	-	30.77	38%	24.4	-	254.2	43.31	110.49	28.04	24.39	254.20	45.77	65.65
BR-5	6	Study area	*This study*	-29.216	-49.969	127	Sandstone - Botucatu Fm	Early Cretaceous	29.6	4	67.65	9.99	15%	45.3	-	93.1	61.45	45.25	93.11	70.79			
BR-1	7	Study area	*This study*	-29.582	-50.426	145	Sandstone - Botucatu Fm	Early Cretaceous	40.5	5	105.28	10.80	10%	73.6	-	130.7	115.33	120.34	130.69	86.45	73.57		
BR-2	8	Study area	*This study*	-29.585	-50.281	71	Sandstone - Botucatu Fm	Early Cretaceous	29.2	5	105.48	8.19	8%	81.8	-	130.1	81.80	111.07	94.38	130.05	110.12		
BR-3	9	Study area	*This study*	-29.534	-50.203	261	Sandstone - Botucatu Fm	Early Cretaceous	26.6	5	111.47	13.19	12%	75.2	-	154.2	102.51	123.98	75.18	101.46	154.22		
BR-4	10	Study area	*This study*	-29.534	-50.203	260	Sandstone - Botucatu Fm	Early Cretaceous	26.6	4	101.75	14.12	14%	60.1	-	122.3	122.34	114.76	109.82	60.09			
L-1	11	Study area	Karl et al. 2013	-28.388	-49.508	620	Sandstone - Botucatu Fm	Early Cretaceous	49.0	3	43.13	6.53	15%	32.2	-	54.8	54.80	42.40	32.20				
L-2	12	Study area	Karl et al. 2013	-28.361	-49.306	194	Granodiorite	Neoproterozoic	35.0	3	86.60	12.09	14%	63.2	-	103.6	63.20	103.60	93.00				
L-3	13	Study area	Karl et al. 2013	-28.295	-49.114	133	Granite	Neoproterozoic	24.2	3	79.43	4.17	5%	72.9	-	87.2	87.20	78.20	72.90				

References:

Bertolini, G., Marques, J.C., Hartley, A.J., Da-Rosa, A.A.S., Scherer, C.M.S., Basei, M.A.S., Frantz, J.C., 2020. Controls on Early Cretaceous desert sediment provenance in south-west Gondwana, Botucatu Formation (Brazil and Uruguay). Sedimentology. https://doi.org/10.1111/sed.12715

Canile, F.M., Babinski, M., Rocha-Campos, A.C., 2016. Evolution of the Carboniferous-Early Cretaceous units of Paraná Basin from provenance studies based on U-Pb, Hf and O isotopes from detrital zircons. Gondwana Research. https://doi.org/10.1016/j.gr.2016.08.008

Donelick, R.A., 2005. Apatite Fission-Track Analysis. Reviews in Mineralogy and Geochemistry. https://doi.org/10.2138/rmg.2005.58.3

Gautheron, C., Tassan-Got, L., Barbarand, J., Pagel, M., 2009. Effect of alpha-damage annealing on apatite (U–Th)/He thermochronology. Chemical Geology 266, 157–170. https://doi.org/10.1016/j.chemgeo.2009.06.001

Gerin, C., Gautheron, C., Oliviero, E., Bachelet, C., Mbongo Djimbi, D., Seydoux-Guillaume, A.-M., Tassan-Got, L., Sarda, P., Roques, J., Garrido, F., 2017. Influence of vacancy damage on He diffusion in apatite, investigated at atomic to mineralogical scales. Geochimica et Cosmochimica Acta 197, 87–103. https://doi.org/10.1016/j.gca.2016.10.018

Gomes, A.S., Vasconcelos, P.M., 2021. Geochronology of the Paraná-Etendeka large igneous province. Earth-Science Reviews. https://doi.org/10.1016/j.earscirev.2021.103716

Ketcham, R.A., Carter, A., Donelick, R.A., Barbarand, J., Hurford, A.J., 2007. Improved modeling of fission-track annealing in apatite. American Mineralogist 92, 799–810. https://doi.org/10.2138/am.2007.2281

Ketcham, R.A., Gautheron, C., Tassan-Got, L., 2011. Accounting for long alpha-particle stopping distances in (U–Th–Sm)/He geochronology: Refinement of the baseline case. Geochimica et Cosmochimica Acta 75, 7779–7791. https://doi.org/10.1016/j.gca.2011.10.011

Milani, E.J., de Melo, J.H.G., de Souza,P.A., Fernandes, L.A., França, A.B., 2007. Bacia do Paraná Bol. Geociencias Petrobras, 15 (2), pp. 265-287.

Recanati, A., Gautheron, C., Barbarand, J., Missenard, Y., Pinna-Jamme, R., Tassan-Got, L., Carter, A., Douville, E., Bordier, L., Pagel, M., Gallagher, K., 2017. Helium trapping in apatite damage: Insights from (U-Th-Sm)/He dating of different granitoid lithologies. Chemical Geology 470, 116–131. https://doi.org/10.1016/j.chemgeo.2017.09.002

Wygrala, B. P., 1989, Integrated study of an oil field in the Southern Po-basin, Northern Italy (Ph. D. Thesis): University of Köln. (Ber. Forschungszentrum Jülich 2313, 217 pp.)